A Novel THz Photoconductive Source and Waveguide Based on One-dimensional Nano-grating

by

Saman Jafarlou

A thesis
presented to the University of Waterloo
in fulfillment of the
thesis requirement for the degree of
Master of Applied Science
in
Electrical and Computer Engineering

Waterloo, Ontario, Canada, 2013

I hereby declare that I am the sole author of this thesis. This is a true copy of the thesis, including any required final revisions, as accepted by my examiners.

I understand that my thesis may be made electronically available to the public.

Abstract

A terahertz photoconductive source structure with nano-grating electrodes is proposed. The resonance modes of the one-dimensional nano-grating and their affect the optical power absorption are studied. In addition, an approach for optimal design of the grating to maximize the photocurrent for different proposed DC biases, is presented. The dependence of the photocurrent on physical parameters of photomixer are analyzed.

A fast analysis method for a new terahertz waveguide for photo-mixing is proposed. The wave-guiding mixer structure is a modified parallel plate waveguide (PPWG) in which the top plate is replaced by a periodic array of sub-wavelength nano-slits. The substrate of the PPWG is made of a fast photoconductive material in which laser photomixing/absorption occurs. The characteristic equation of the modified PPWG when used as a THz waveguide is derived analytically, and its guided modes are studied in details over THz range of frequencies. The accuracy of the analytical results are verified by comparison with full-wave numerical simulations. The criteria for choosing the suitable mode for photomixing application are also discussed. Finally, based on dyadic Greens function representation, a systematic approach is provided for calculating the amplitude of the guided modes that are excited by an arbitrary photocurrent.

Acknowledgements

I would like to express my sincere gratitude to my supervisor, Professor Safieddin Safavi-Naeini for his invaluable guidance, encouragement, and support. I really appreciate his endless kindness, patience, and help during my graduate study.

I also would like to thank Dr. Mohammad Neshat for his valuable directions and discussions during the course of this research.

This research was supported by National Science and Engineering Research Council (NSERC) of Canada and Research In Motion (RIM).

Dedication

This is dedicated to my father and mother for their endless support, to my brother and to my love.

Table of Contents

List of Tables

List of Figures

Chapter 1

Introduction

1.1 State of the Art

Range of frequency between 300GHz to 3THz is known as THz range shown in Fig. 2.2, also called millimeter wave. This Range of electromagnetic spectrum has unique properties including transparency to verity of materials and sharp resonance of most polar molecules. These features bring various application that can fall in two major group: Screening and Spectroscopy application.

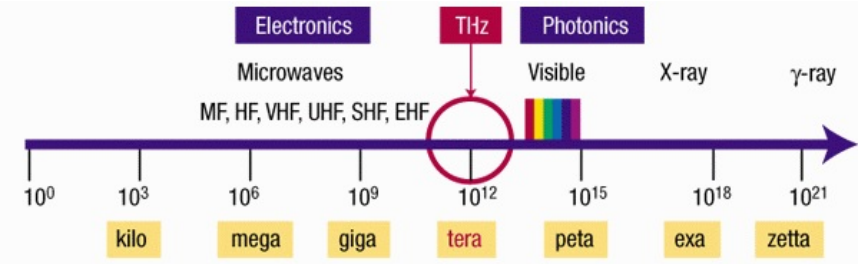

Figure 1.1: Electromagnetic spectrum and THz gap

THz radiation can easily penetrate the optically opaque material such as plastic and thin clothing. This potential capability for detection of non-metallic concealed weapons has attract enormous attraction in security application. Basically, non-metallic object cannot be revealed under established X-ray imaging methods, in addition low energy of THz photons provide harmless imaging technique on living tissue in contrary to X-ray imaging.

Signature frequency fingerprint of most compound substances, particularly biological material, is due to rotational eigenstates of this molecules with a eigenfrequency in THz range. As the resonances of originated from this sharp rotational resonances are very sensitive to molecule's type, such sensitivity can be combined with THz imaging technique to identify organic molecules in a solution.

Transparency of THz, boost a its novel astronomical application to monitor the cosmic radiations. The main motivation is "approximately one-half of the total luminosity and 98% of the photons emitted since the Big Bang fall into the submillimeter and far-infrared" [2]. Moreover, the optical light emitted in spatial phenomena usually are blocked by stellar dust, thus the detecting other THz range of the radiation will be impressively helpful in astronomical studies. These three main application of THz technology is shown in Fig. 1.2.

Despite of this prospective on application of THz, lack of a reliable THz signal generator hinder the extensive development of this field from practical point of view."THz gap", which is a common word in community of electromagnetic and photonics, indicates this fundamental challenge in this area. During the past decades, several research center devoted to improve the efficiency of the THz sources to bridge the THz gap.

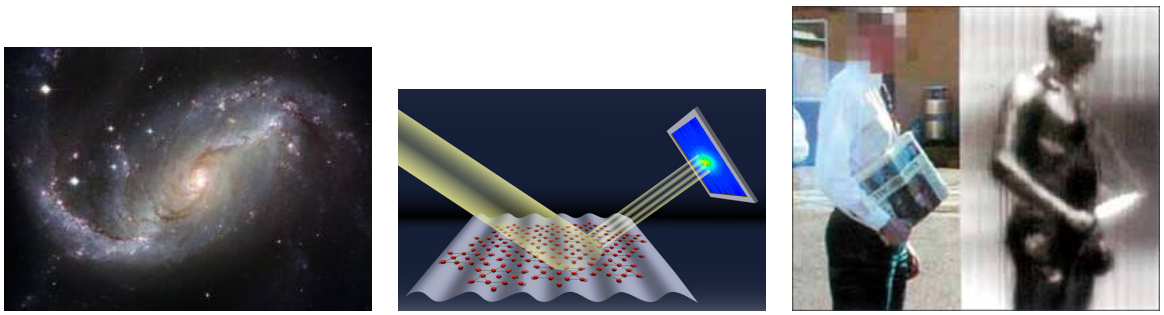

(a) (b) (c)

Figure 1.2: THz Application in a)astronomy b)spectroscopy (picture courtesy to Max Planck Structural Dynamics) c)surveillance imaging

1.2 Motivation and Objective

The major challenge in generating THz single in current technological infrastructure is the inverse relation between the power of the source and its operational condition. Some

proposed THz sources with relatively high power, such as quantum casdcade lasers and superconductive sources, are operate in extremely low temperature. Although some high-temperature sources are developed recently, but there is still undeniably far from operating in room temperature. On the other hand, the photoconductive sources, which work in common temperatures, have very lower output power. Numerous factors hinder the these to give considerable power, which lays in physics of photomixing phenomenon and technological limitation. For example, the component of the current that is responsible for THz radiation produced by the optical absorbed power. We have proposed a nano-scaled plasmonic grating to localized the optical field to increase power absorption in the photoconductor. We also study the coupling of THz power to the grating, which can be used in integrated application.

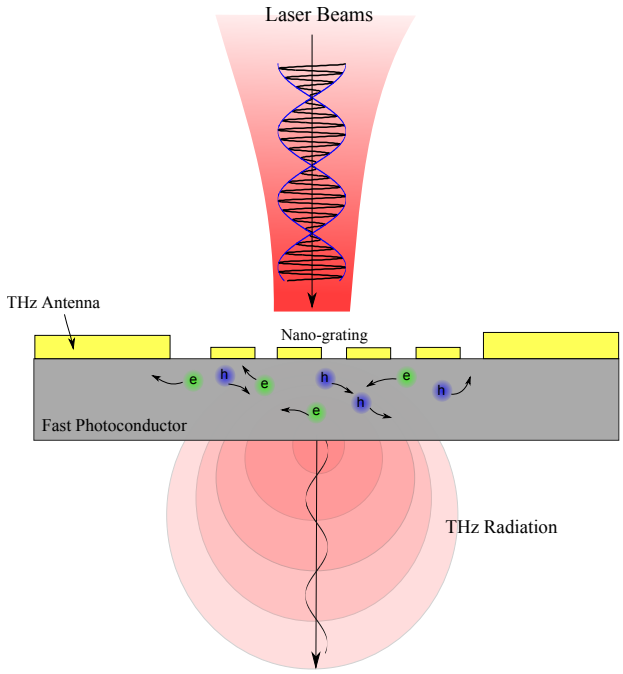

Figure 1.3: Proposed Photomixing Structure

1.3 Thesis Outline

This thesis is organized based on the physical consequence of photomixing phenomenon. Two optical field with frequency falling in THz range are mixed in a photoconductive

material, which leads to generate a photocurrent osculating with Thz frequency. Thus after presenting a brief review on previous works on various techniques to produce THz field

In chapter 3, the method the photomixing is investigated from photonic point of view. I other words, the distribution of optical field caused by an incident optical beam on a one-dimensional metallic grating is studied. Thus, the absorbed photon density in the photoconductive substrate is obtained, which is proportional to released carrier density. Obtained carrier density is employed to find the photocurrent flow in substrate, through drift diffusion model.

In chapter 4, using the THz photourrent obtained in previous chapter, an analytical method is presented to calculate the coupled field into the THz waveguide and radiated field.

1.4 Publications

- **S. Jafarlou**, M. Neshat and S. Safavi-Naeini, "A Fast Method for Analysis of Guided Wave and Radiation from a Nano-scale Slit Loaded Waveguide for a THz Photoconductive Source," *IEEE Trans. on Terahertz Science and Technology* , vol. 2, no. 6, Nov. 2012.

- **S. Jafarlou**, M. Neshat and S. Safavi-Naeini, "Enhanced Terahertz Photomixing Based on Resonance Modes of One-dimensional Nano-grating," (to be submitted).

Chapter 2

Review on THz technology

THz range is one of the intervals in electromagnetic spectrum which has been least explored. Lack of a reliable and high-power source and sensitive detector, impede more practical research and works in this area. In this chapter a brief review on various works to overcome this shortage is presented.

2.1 Optical and Microwave Approaches for THz Generation

Efforts to bridge THz gap by developing effective source falls in two major categories as illustrated in Fig. 2.1 . First, efforts to boost the operational frequency of the current microwave techniques. Second, generating THz signals based on optical methods such as photomixing and lasing.

Electronic solid-state sources are working as frequency multiplier using semiconductor junctions based devices such as Gunn and IMPIAT diodes [3]. Other conventional frequency multipliers generate higher order harmonics of the feed frequency through a nonlinear devices. This nonlinear effect can be due to Shottkey effect in Planar-Shottkey varactor diodes. This method generally have low signal to noise ratio, because of high noise involved in nonlinear process, besides the nonlinear effect limits the maximum achievable frequency.

Quantum cascade lasers(QCL) are semiconductor laser developed for THz emission. It is working by intersubband transitions in a repeated stack of multiple quantum well

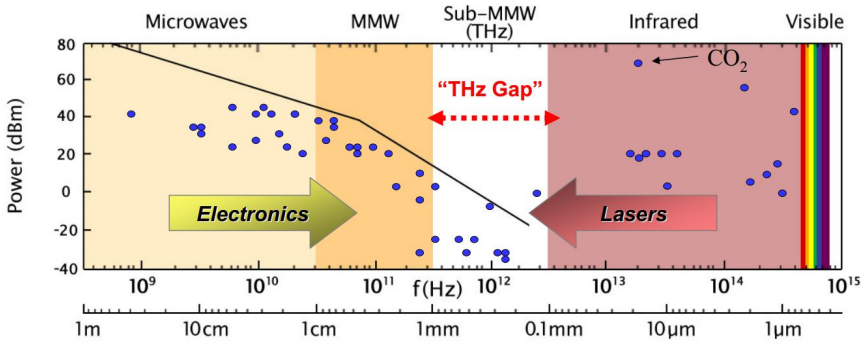

Figure 2.1: Optical and eletronic optical appproaches to THz technologies (courtesy, Dr. Mark Rosker, DARPA)

heterostructures. The main challenge in these lasers are decreasing the operation frequency to THz range, as well as increasing output power. The very low operation temperature of QCL, require bulky cooling system that prevents the widespread application of QCL.

THz free electron laser (FELs) source, which generate signal based on interaction of high-energy oscillating electrons beam, result in relatively high output power. The large size and heaviness of the cooling system and magnetic field coil of these devices is their primary disadvantage[4]. Far-infrared lasers (FIR) are also, proposed for THz generation. FIRs consist of long cavity filled with pumped gas that lases in present of strong magnetic field at THz range, like CO_2. These laser are inefficient in terms of high operation power for cooling system and applying magnetic fields.

The other promising optical technique for THz generation is photomixing in either ultra-fast photoconductor or nonlinear crystal. Exciting a nonlinear process by a two optical beam offset by the THz frequency, generate higher order harmonics which include component varying in THz frequency. The nonlinear process can be emanate from a nonlinear polarization response χ of a crystal to intense electrical field. High optical intensity need to affect slight nonlinearity of crystals such as lithium-niobate and zinc-telluride often limits this technique to pulse generation. The nonlinear process is photoconducting phenomenon in which the carrier density, and consequently photocurrent, are proportional to optical average illuminating the material. Thus, the photocurrnet includes THz component that radiates THz signal.

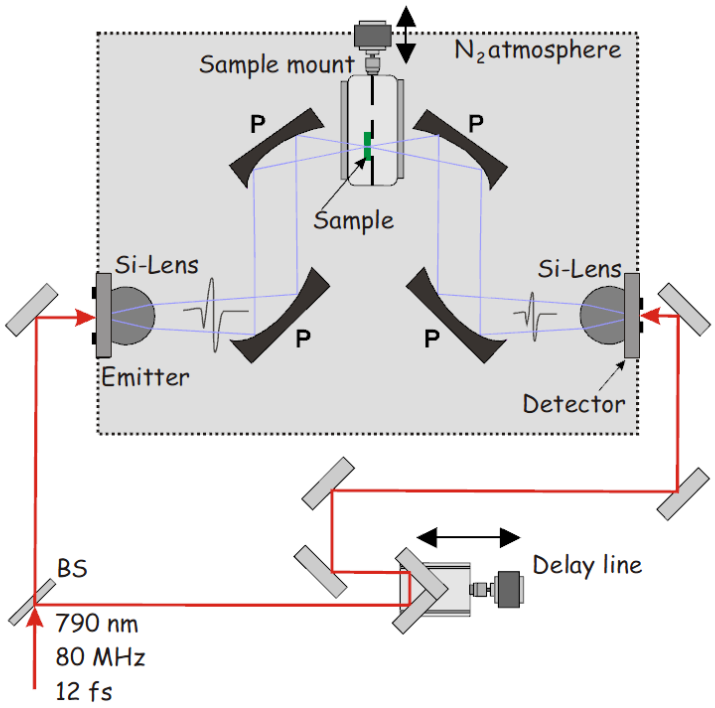

Figure 2.2: A typical pulse-regime THz spectroscopy setup

2.2 Pulse and Continuous-wave THz Photomixing

Mixing of two optical beams to generate THz signal can be done in two regime: pulse and continuous-wave (CW) THz generation. In the former, illumination is done by a femtosecond laser pulse, whereas the a continuous laser beam is used in latter one. Photoconductive source in pulse generation is usually referred as photoconductive switch. A photoconductive switch consist of a high resistive material, e.g. GaAs, which can rapidly turns into a conductive medium by releasing a large number of carriers in a short period of time. The abrupt change in conductivity result in creation a broad range of frequencies in electromagnetic spectrum. This spectrum radiates into free space after passing a low pass filter imposed by antenna. The maximum frequency exist in output power is dictated by the badwidth of antenna, equivalent capacity at the illumination spot and the carrier lifetime of the photoconductor.

By applying a continuous laser beam on the photoconductor switch will lead to radiating a coherent continuous-wave THz signal. Equilibrium condition exist in CW mode allow

a reliable analysis based on the carrier transport model in semiconductors, which are not applicable in pulse mode.

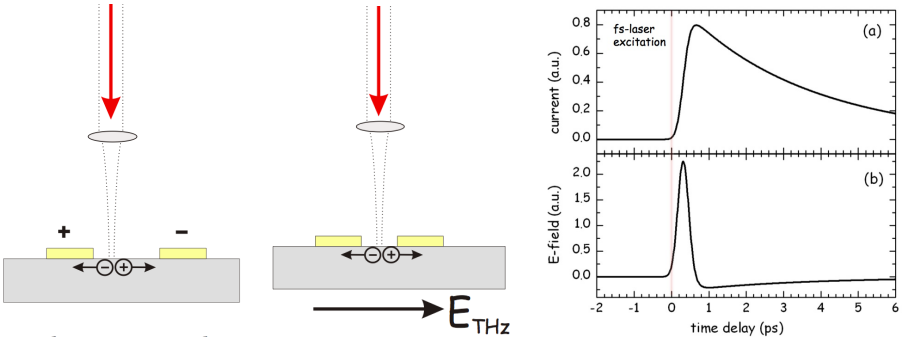

(a) (b) (c)

Figure 2.3: schematic view of the a) emitter and b) detector in THz spectroscopy setup, c) the photocurrent and THz field with respect to time delay.

2.2.1 Pulse generation and detection in THz spectroscopy

Fig. 2.2 shows a schematic view for the THz time-domain spectrometer setup. A femtosecond pulse of a laser beam is driven through reflective mirrors and a beam splitter to the THz emitter and detector, which both can be an identical THz photoconductive antennas. Short electromagnetic pulse is led through the sample using the paraboloidal mirrors. The transmitted radiation signal and delayed optical laser pulse illuminate the detector from two sides.

By focusing of a femtosecond laser pulse light on antenna gap of the photoconductive emitter, the gap becomes conductive extremely fast (below a ps), and the subsequent electorn and holes get separated under the DC bias giving a current between electrodes as shown in Fig. 2.3(a). The produced current decay due to the recombination of the carriers with an average lifetime of the substrate (around 2 ps), this varying current result in a electromagnetic radiation which is approximately proportional to the time derivative of the current, shown in Fig. 2.3(c). In the case of fast photoconductive material (short carrier lifetime) the spectrum of the radiated field contain a significant component in THz range.

In Fig. 2.1(b) the mechanism of THz detection is illustrated. The carriers generated by the delayed optical pulse are accelerated toward the electrodes due to the captured THz

signal. The current in the probes of the detector is measured to evaluated the amplitude of the time-domain response of the sample. By varying the time delay of the optical pulse, which act as a probe signal, the electric field variation with respect to time-delay can be found. The Fourier transform of this response presents the unique signature of the sample which may include some monocular resonances.

2.2.2 Continuous-wave THz generation

As shown in Fig. 2.4, two laser beam at frequencies at f_0 and $f_0 + f_{\mathrm{THz}}$ with same polarization, illuminating the gap of photoconductive antenna result in a total optical intensity of

$$I(t) = E_1^2 + E_2^2 + 2E_1E_2\cos(2\pi f_{\mathrm{THz}}t) \tag{2.1}$$

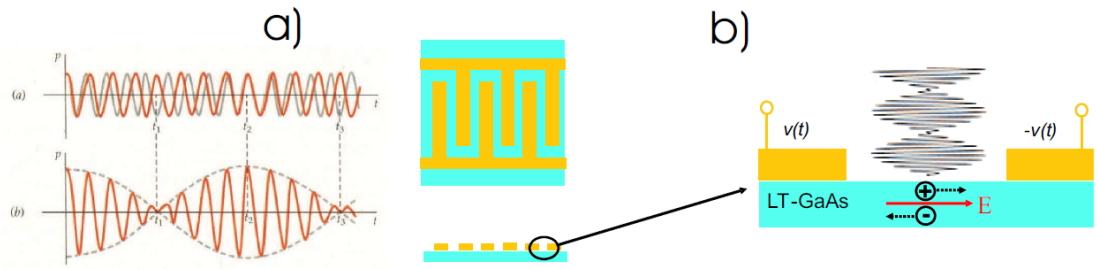

Figure 2.4: Schematic discription of CW THz generation

For sufficiently high f, the optical absorbed power leads to creation of electrons and holes in the photoconductor, with a rate proportional to the optical intensity. Due to optical modulation, the current contain an AC component with f_{THz} frequency. Phase matching of the signal is not of importance because of the short absorption length of photoconductor and highly focused optical beam. An THz antenna is employed to convert the AC photocurrent in the gap to a efficient free space radiation. Due to lower impedance of substrate in comparison with air impedance, most of the power will radiate into the substrate. For efficiently capture the radiated power a hyperhemispherical high-resistive silicon is mounted to the other side of the substrate as shown in Fig. 2.5(a).

Antenna used in the photomixers has a critical impact on the frequency response and amplitude of the THz radiation. Typically broadband antennas, such as spiral and bow-tie antennas (Fig. 2.5(b)) , are more popular in photomixers. However, the $\lambda/2$-dipole

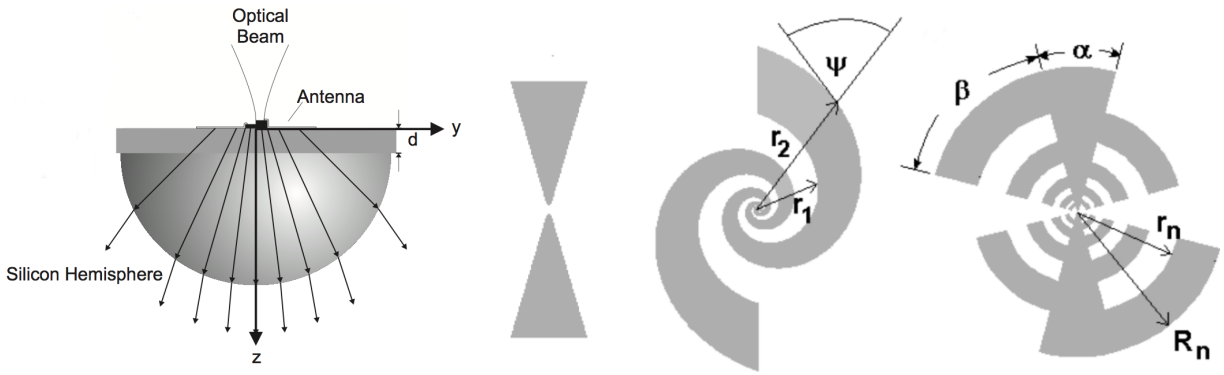

(a) (b)

Figure 2.5: schematic view of the a) emitter and b) detector in THz spectroscopy setup, c) the photocurrent and THz field with respect to time delay.

antenna is vastly used to investigate the performance of photomixing phenomenon. The radiation impedance of the antenna ($Z_A = R_A(\omega) + jX_A(\omega)$) should be matched to the equivalent impedance of gap to maximum coupling of THz wave occurs. The Imaginary part which corresponds to the energy stored in near field, vanishes when the resonance occurs. Moreover, the radiation resistance has maximum in the resonance condition. Z_A for an antenna lies on a substrate with electrical permittivity of ϵ_r is approximately scaled by factor $\sqrt{(\epsilon_r + 1)/2}$ compared to that of an antenna in free space.

For an ideal radiator, the output power is given by

$$P_{THz} = \frac{1}{2} R_A I^2 \tag{2.2}$$

where I is the generated photocurrent. However, in a real photomixers some additional terms appear to model the high frequency effects. These roll-off terms that decrease the performance of the devices include:

- An RC roll-off term that correspond the RC equivalent circuit of in the antenna input. It consist of the capacitance between the bias electrodes C in antenna gap and radiative resistance R_A of antenna, which are parallel to each other. As a result the power is reduced by a roll-off factor of

$$\eta_{RC} = \frac{1}{1 + (2\pi f R_A C)^2} \tag{2.3}$$

- Lifetime roll-off term is added to model the limitation of the carrier dynamics in the photoconductor. The generated carriers remains in conduction band for an average carrier lifetime τ_{rec} and destructively interfere with the generated carriers of subsequent THz periods. It can be described by the reduction factor of

$$\eta_{rec} = \frac{1}{1 + (2\pi f \tau_{rec})^2}. \tag{2.4}$$

- Average transit time, τ_{trans}, that is needed to carriers reaches to the electrodes, is another time constant of the system particularly for large separation of the contacts. The corresponding roll-off factor is expressed as

$$\eta_{trans} = \frac{1}{1 + (2\pi f \tau_{trans})^2}. \tag{2.5}$$

As it has been discussed before the conductance of the antenna gap, $G(t)$, is modulated in time with THz frequency.

$$G(t) = eN(t)\mu_e \tag{2.6}$$

where e is electron charge and μ_e is electron mobility. Several assumptions has been made here. First, only electrons play role in carrying current, second, the drift current has linear relation with bias field. From the charge continuity equation in equilibrium condition, the carrier density, $N(t)$, can be found

$$\frac{\mathrm{d}N(t)}{\mathrm{d}t} = \frac{\eta P_{opt}}{h\nu} - \frac{N(t)}{\tau_e} \tag{2.7}$$

where $h\nu$ is the photon energy, η is the total quantum efficiency and τ_e is the free-carrier lifetime (which approximately is). By solving Eq. (2.7), conductance of gap is expressed as

$$G(t) = G_0[1 + \frac{2\sin(2\pi f_{THz})}{\sqrt{1 + (\omega\tau_e)^2}}] \tag{2.8}$$

Using this conductance an equivalent circuit for operation of THz photomixer is proposed as shown in Fig. 2.6. The circuit consist of input impedance of antenna, R_A, parallel to the RC model for the gap, including time-varying conductance, $G(t)$, in parallel with gap capacitance. This circuit is fed by the DC bias source V_b.

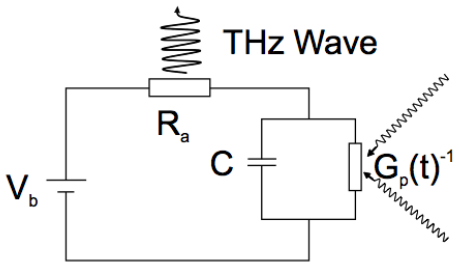

Figure 2.6: The equivalent circuit of the photomixer in CW regime

The radiated power, which corresponds to the power dissipated in R_a, yields from the equivalent circuit:

$$P(t) = \frac{\frac{1}{2}(G_0 V_b)^2 R_a}{(1+\omega\tau_e)^2(1+\omega R_a C)^2} \tag{2.9}$$

2.3 Bias Configurations in the Photomixers

Three possible configuration for electrodes in a photomixing can be presumed, shown in Fig. 2.7. In the

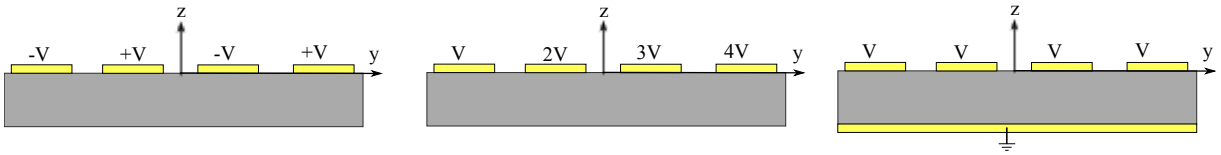

Figure 2.7: Three bias configurations of the electrodes in photomixers: alternating bias (left), incremental bias (middle), vertical bias (right).

Solution of Poisson equation for these structure can be found analytically assuming sufficiently low thickness of the metallic strips. Electric field in y-direction is given by [5]

$$E_y = \sum_{n=0}^{\infty} A_{2n+1} \cos[(2n+1)(\frac{y}{d} + \delta_n)] \exp[(2n+1)\pi\frac{z}{d}] \tag{2.10}$$

where d is the period of the strips, and A_n is the coefficient that are determined by the boundary condition. E_y has a periodic behavior in along y-axis and it is decaying as z

increases, with coefficient proportional to pi/d. In the incremental bias, there is a constant bias filed along y-axis as well as the similar decaying behavior.

$$E_y = \frac{V}{d} + \sum_{n=0}^{\infty} A_{2n} \sin[2n(\frac{y}{d} + \delta_n)] \exp[2n\pi\frac{z}{d}] \tag{2.11}$$

where A_n and δ_n are amplitude and phase constants, respectively.

Chapter 3

Plasmonic Enhancement of Photomixing

3.1 Introduction

Optical properties of one-dimensional (1-D) nanoscale metallic grating and some interesting phenomena, such as the extraordinary optical transmission (EOT) introduced by Ebbesen et al. [6] have been studied in numerous works over the last decade. Considerable amount of research efforts have been dedicated to develop theories underlying EOT, in which, this phenomena is described by the excitation of transverse resonance modes of the grating that occur for different geometries at certain frequencies. On the other hand, optical field enhancement of light at the vicinity of grating stimulate the exploration the applications of 1-D metallic grating in optical devices such as metal-semiconductor-metal (MSM) photodetectors [7] and optical waveguides [8].

Very recently, there has been an increasing interest in applying such grating to enhance the efficiency of the terahertz photocunductive switch [9] [10] for continuous-wave and pulse emission, respectively. These works report the measurement result for two configuration of photoconductive source, in addition to brief discussion on grating design approach and choice of bias, independently. In [11] and [12], nanoantenna is employed to enhance optical absorption in THz emitters by surface plasmonic localization of light. Besides, Tanoto et al. have recently reported significant enhancement continuous-wave terahertz emission by adopting plasmonic effects of interdigitated nano-electrodes. From the design perspective, an inclusive analysis is required which incorporate optical scattering, carrier dynamic and

THz radiation problems simultaneously. We have analyzed THz radiation due to a current source in presence of nanograting in [13].

Scattering problem of 1-D subwavelength metallic grating on absorbing substrate has been well treated in literature for different applications. For example, absorption profile of this grating on silicon substrate is investigated through FEM calculation for MSM and solar cell applications in [14]. Furthermore, enhancement of optical absorption is studied within visible light range for periodic metallic grating on the top of the organic solar cells [15].

Various theoretical models has also been proposed to describe carrier dynamics in photomixers, e.g., nonequilibrium Boltzmann equations [16], Drude-Lorentz models [17] and standard drift-diffusion equations [18] [19]. In this paper we have used the last one, which is more popular to analyze photomixers in continuous-wave regime.

In this paper, a terahertz photoconductive source structure with nano-grating electrodes is analyzed, and a numerical approach is presented to design the nano-scaled grating to maximize the photocurrent for different electrode configurations. An overview on the resonance modes of the metallic grating is presented and the results of different analysis are compared in Section 3.2. optical absorbed power enhancement in the photoconductor substrate at wavelength 800nm for different grating geometries is studied in Section 3.3. In Section 3.4, the photocurrent created under three bias configurations is obtained from standard carrier transport calculations. Section 3.5 concluded the paper.

3.2 Optical Transmission Through 1-D Metallic Grating

One-dimensional metallic grating, which we use in photoconductor source, consists of periodic gold strips with thickness h, periodicity d, and width a on a substrate made of a photoconductive material as shown in Fig. 3.1(a). We define height ratio and filling factor as h/d and w/d, respectively. In this paper, we restrict our study to TM polarized (magnetic field parallel to the grating) laser beam impinging on the grating plane in perpendicular direction. In addition, the laser beam spots are assumed large enough so that the incident laser beams can be modeled as plane waves.

In this Section, we compare different optical transmittance analysis for 1-D metallic grating illuminated by a single frequency plane wave. A discussion on transmission resonance modes is provided in [1] based on zeroth order transmission coefficient T_0 , obtained

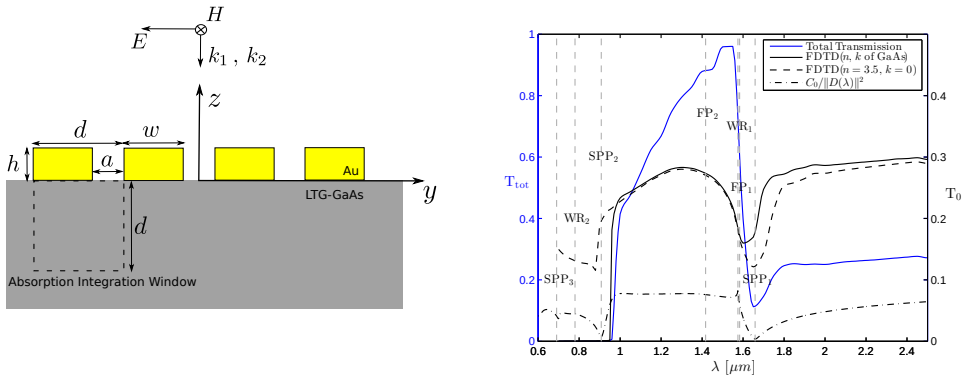

(a) (b)

Figure 3.1: a) Schematic view of the structure and the intergration window for optical absorption calculation, (b) zeroth order transmission obtained from Eq. 1 in [1] with arbitrary coefficient C_0 and FDTD method for absorbing and non-absorbing substrate for grating dimension of $d = 450$nm, $h = 300$nm, $w = 300$nm. FDTD results for total power transmission is also plotted. Vertical dashed lines shows the location of WR anomalies, SPP and CM resonances obtained as explained in the text.

from the transfer matrix method, [20], with the assumption of surface impedance boundary condition (SIBC) for horizontal metal surfaces and perfect conductor for slit's vertical walls, and single-mode propagation inside the slit. The analytical expression for denominator of the zeroth order transmission (Eq. 1 [1]) allows one to identify the modes that play important roles in the optical response as following:

1) Wood-Rayleigh (WR) anomalies: abrupt changes in transmittance due to the emergence and vanishing of the diffraction orders from a metallic grating. WR anomalies which depends solely on the geometrical parameters occurs when $\lambda_j^{\mathrm{WR}} = d/j$, where $j = 1, 2, ...$

2) Surface plasmon polariton (SPP): coupling of the Floquet modes of the grating with the surface plasmons of the top and bottom metal-dielectric interfaces, which are almost coincide with WR. SPPs wavelengths are given by $\lambda_j^{\mathrm{SPP}} = d/j\sqrt{\epsilon_m\epsilon_i/(\epsilon_m + \epsilon_i)}$, where $j = 1, 2, ...$ and $\epsilon_i = 1, \epsilon_s$ for top and bottom surface plasmons, respectively, and ϵ_m is electrical permitivity of metal.

3) Cavity Modes(CM): satisfying Fabry-Perot-like resonance condition within the slit leads to channeling of the light through the grating. In [21], a semi-analytical approach based on the method of moment and the expansion of the field inside the slit has been taken to find the zeroth order transmission and reflection coefficients for the sufficiently

thick metallic gratings. This approach carefully takes the channeling properties of the slit into account, and all metallic characteristics of the grating are accounted for the calculation of the effective index(n_{eff}) of the fundamental waveguide mode of the slit that must be determine beforehand. Various methods have been employed to find n_{eff} [22] [20], a simple approximate formula is presented in [23] with acceptable accuracy to predict the location of the transmission peaks.

We also use a finite difference time domain (FDTD) solver, provided by EMW module of Synopsys TCAD [**?**], in order to solve this optical scattering problem. In FDTD solver, Lorentz-Dude model [24] is used for gold, and optical parameters for LTG-GaAs are obtained from [25].

Fig. 3.1(b) shows zeroth order transmission obtained from Eq. 1 in [1], where the location of WR anomalies, SPP and CM resonances are found from the aforementioned discussion. FDTD simulation shows a good agreement for the case of a constant refractive index for the substrate $n = 3.5$. This simulation is repeated for LTG-GaAs substrate with real optical parameters which are wavelength dependent and showing high absorption for wavelength below 950nm. It can be observed that for this case transmittance deviates slightly at higher wavelengths and drops rapidly to zero at wavelengths shorter than that corresponding to the GaAs energy band-gap. Total transmitted optical power for real LTG-GaAs is also plotted in Fig. 3.1(b) showing it has same peaks and dips as T_0.

3.3 Optical Absorption of 1-D Grating

Time-averaged optical absorbed power in each point of photoconductive substrate due to single beam is given by $P^I_{ave} = \epsilon''|E|^2/2$. While in terahertz photomixer, two optical plane waves with frequencies of f_0 and $f_0 + f_{\text{THz}}$ generate an average optical absorbed power modulated by the difference frequency of f_{THz} as

$$P^{II}_{ave}(t) = P^I_{ave}(1 + m\cos(2\pi f_{\text{THz}} t)) \tag{3.1}$$

Here m is the modulation index. Absorbed optical power multiplied by quantum efficiency (η) leads to optical generation rate, which is a crucial parameter in efficiency of THz photomixers. In this Section, we study the optical absorbed power due to single beam for different grating dimensions, in which various resonance modes may occur. In order to have a quantitative measure for comparison between various resonance modes, we take the spatial average of the optical absorbed power, $\bar{P}_{ave} = 1/d^2 \int_{\text{win}} P^I_{ave}\, \mathrm{d}S$, over a window with

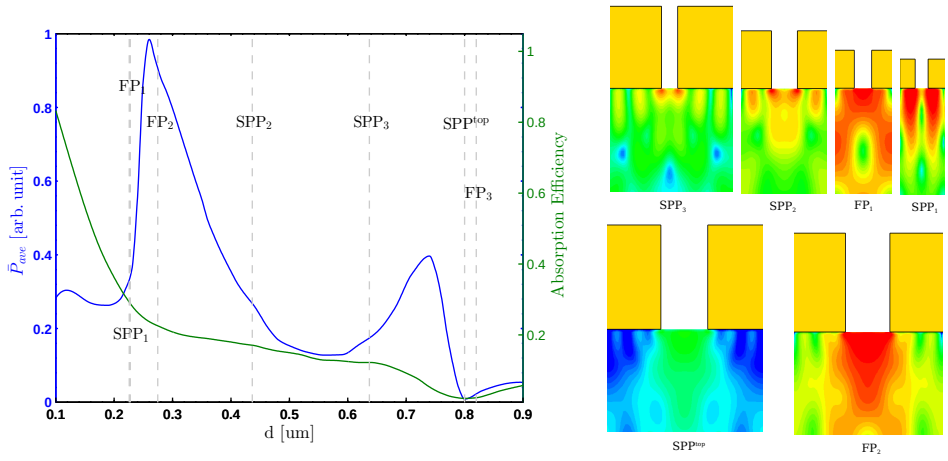

(a) (b)

Figure 3.2: a) Spatial average of the optical absorbed power and absorption efficiency (ratio of power absorbed in substrate over power dissipated in metals) with respect to grating period when $h/d = 0.7$ and $w/d = 0.67$ at 800nm wavelength, b) optical absorption density profile for resonance modes in (a).

one period of grating as shown in Fig. 3.1(a). This choice can be justified by noting that bias electrical field of alternating or incremental voltages applied to the strips (see Section 3.4) is approximately decaying with $e^{-\gamma|z|/d}$, where γ is a constant , thus generally carriers generated close to surface have more contribution to photocurrent due to high bias field in vicinity of grating.

In Fig. 3.2(a), the spatial average of absorbed optical power in the substrate is shown with respect to grating period obtained from FDTD simulation, where the filling factor and height ratio are kept constant. Resonance modes for the zero order transmission obtained from the theoretical model is also plotted in Fig.3.2(a). Since WR and SPP resonances occurs very close together, we only indicate SPP on the figures. It shows that the optical absorbed power peaks are highest at FP resonance, and then drops rapidly to very low value at the air-gold interface plasmonic resonance at air/gold surface. It is also interesting to note that optical absorption also decreases at lowest order substrate-gold SPP resonance (SPP_1), but higher orders SPP_1 and SPP_2 do not show the similar behavior.

Absorption efficiency can be defined as the ratio of the optical absorbed power in the substrate to the power dissipated in gold. Fig. 3.2(a) shows that the absorption efficiency decreases as the grating period increases. Intuitively, it is because of increasing size of

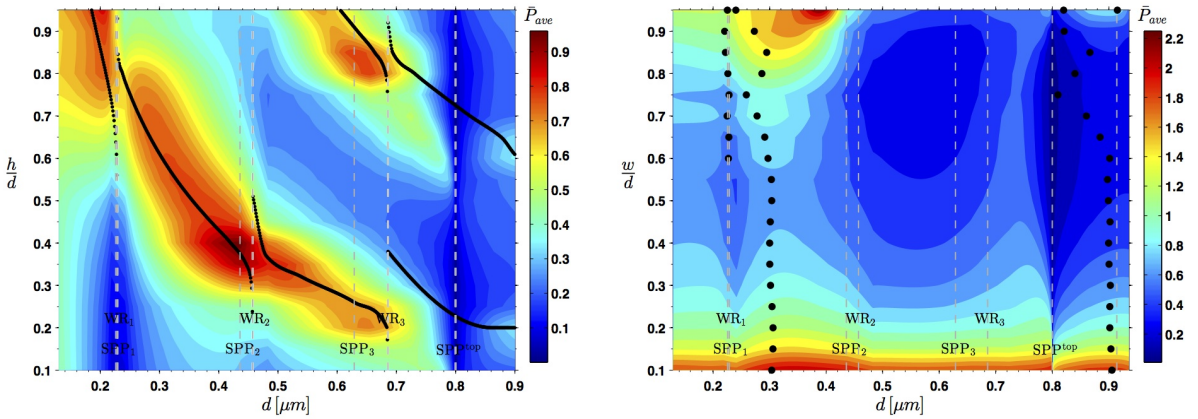

(a) (b)

Figure 3.3: Contour of average optical absorption density in the window shown in Fig. 3.1 (a) with respect to (a) height ratio (h/d) when $w/d = 0.67$, (b) filling factor (w/d) when $h/d = 0.7$ and grating period d. The location of FP resonances are also plotted (black dots).

metals in terms of wavelength (or skip depth of metal), which leads to higher amount of field presented in metal.

Fig. 3.2(b) illustrates the P_{ave} distribution for various grating periods in which the transmission resonance occurs. It can be observed that in FP resonances most of the power is absorbed under the slit, while for SPPs absorption occurs within a lobes under the metals and the number of these lobes is the order of SPPs. Absorption within these lobes is only significant in first resonance (SPP_1).

The dependency of $\bar{P}_{ave}$ to grating dimension is presented in a more general form in Fig. 3.3. Fig. 3.3(a) shows that the optical absorbed power has a peak on the locus of FP resonance [14], where as it has a dip in the location of SPP^{top} which prevent optical power to penetrate into the substrate. It is interesting to note that points of intersection of SPP and FP locus are $\bar{P}_{ave}$ upsurge dramatically. This behavior can be observed in Fig. 3.3(b), in addition, $\bar{P}_{ave}$ generally rise as the filling factor (w/d) decreases.

3.4 Carrier Transport Analysis

The optical generation rate given by $G = \eta P_{ave}^{II}(t)/hf_0$, where h is Plank's constant, is used in solving the coupled electrostatic and carrier transport equations[19] expressed as

$$\nabla.(\epsilon\phi) = q(\rho_n - \rho_p) \tag{3.2a}$$

$$\pm\nabla.\vec{J}_{n,p} = q(G_{opt} - R) + q\frac{\partial\rho_{n,p}}{\partial t} \tag{3.2b}$$

$$\vec{J}_{n,p} = -q\,\mu_{n,p}\,\rho_{n,p}\,\nabla\phi \pm q\,D_{n,p}\,\nabla\rho_{n,p} \tag{3.2c}$$

Where n and p signify electron and hole respectively, ϕ is electrostatic potential, ϵ is electrical permittivity, ρ is charge density, D indicates diffusion coefficients, μ is carrier mobility and R is carrier recombination rate. These sets differential equations are solved in SDevice module of Synopsys TCAD self-consistently in an iterative manner [**?**]. In the simulated model, gold-GaAs interface is assumed as ohmic contact implying infinite surface recombination velocity[26]. Shockley-Read-Hall (SRH) and Auger carrier recombination [27] considered. Zero-field life time for electron and hole are assumed 0.2 ps and 0.9 ps, respectively [28]. In addition, mobility and lifetime saturation due to high electric field, described in [29], are incorporated in the simulations.

Generated carrier flows within drift and diffusion processes to create a current, thus this terahertz time dependency is conveyed to photocurrent. Ultimately, time-dependent photocurrent, $\vec{J}_{ph}(t) = \vec{J}_n + \vec{J}_p$, also has similar time dependency at any arbitrary point

$$\vec{J}_{ph}(t) = \vec{J}_{DC} + \vec{J}_{AC}\cos(2\pi f_{\mathrm{THz}}\,t) \tag{3.3}$$

Where $\vec{J}_{AC}$ and $\vec{J}_{DC}$ are AC and DC component of the photocurrent at the point. It is apparent that desired component is J_{AC} which oscillates with f_{THz}. The generated carriers can be manipulated by applied bias to flow in the desired direction. Therefore proper choice of the bias configuration for each resonance mode is of great importance. Fig. 3.4(a) shows three configurations for the bias of the electrodes and the J_{ph} defined for each. Alternating bias, realized by interdigitated fingers, is consecutive toggling of voltage of electrodes to $\pm V_0$ and J_{ph} is the current collected by one of the electrodes [10]. In vertical bias, top electrode are biased at same voltage of $10V_0$ with respect to a ground plane at the $5\mu m$ distance beneath. We have chosen for voltage source and of substrate to achieve currents in the same range as that of other two configurations. This configuration can be realized by a two far apart comb electrodes [9]. In alternating and horizontal configurations the photocurrent obtained per grating period is collected

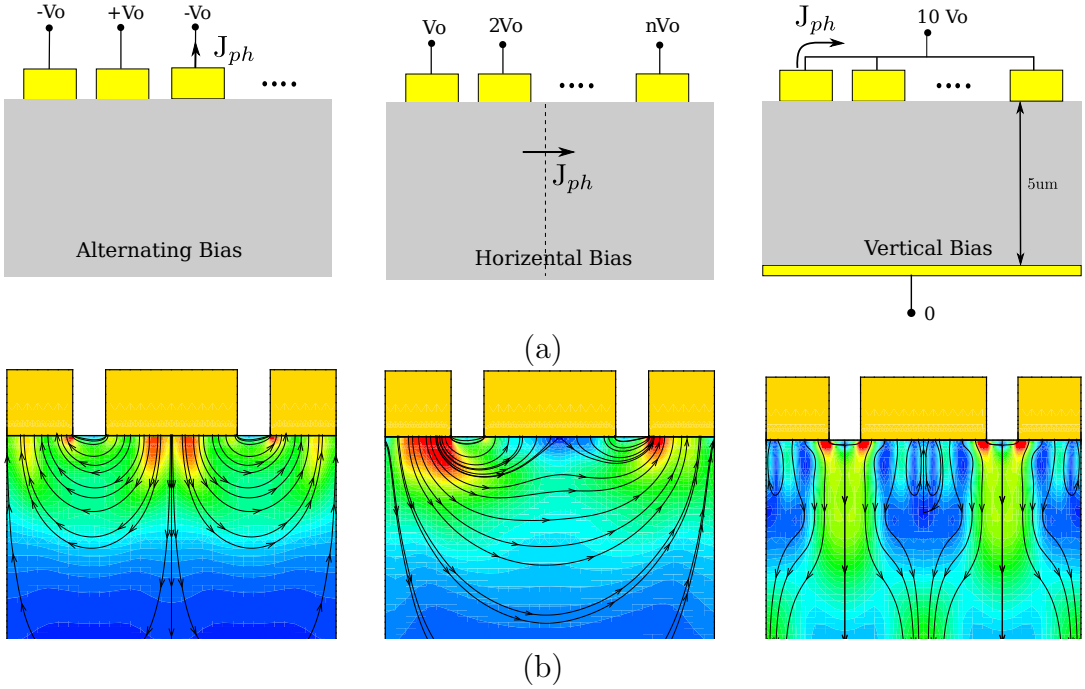

Figure 3.4: (a) Three configuration of biased voltage for electrodes and definition of J_{ph} for each, (b) distribution of AC component of photocurrent, J_{AC}, for corresponding configurations for $V_0 = 2V$, $d = 430nm$, $w/d = 0.8$ and $h/d = 0.4$

current in electrode. In horizontal bias, electrodes are biased by incrementally increasing voltage which cause an overall horizontal electric field. In this case, not only photocurrent can be conducted from electrodes to a THz antenna, but also the photocurrent itself radiates and propagate through grating for sufficiently large grating area [13]. Thus, J_{ph} is considered the total photocurrent flow passed from an arbitrary vertical cross-section. The photocurrent distribution in structure with aforementioned biases are presented in Fig. 3.4(b). In addition to photocurrent values, the capacitance of the electrodes, which yield a RC roll-off term in the frequency response of terahertz emitter [**?**], is a determinant factor in performance of terahertz switches. Capacitance of interdigitated electrodes consist of a parallel set of capacitors between two electrode combs, therefore, there is a tradeoff between the number of finger electrodes and operation speed of device particularly in terahertz pulse generations. While in horizontal bias the capacitance between electrodes are in series, which leads to a lower capacitor by factor $1/N^2$ relatively, where N is number of electrodes.

Photocurrent obtained for different dimensions of the grating is reported in Fig. 3.5(a),

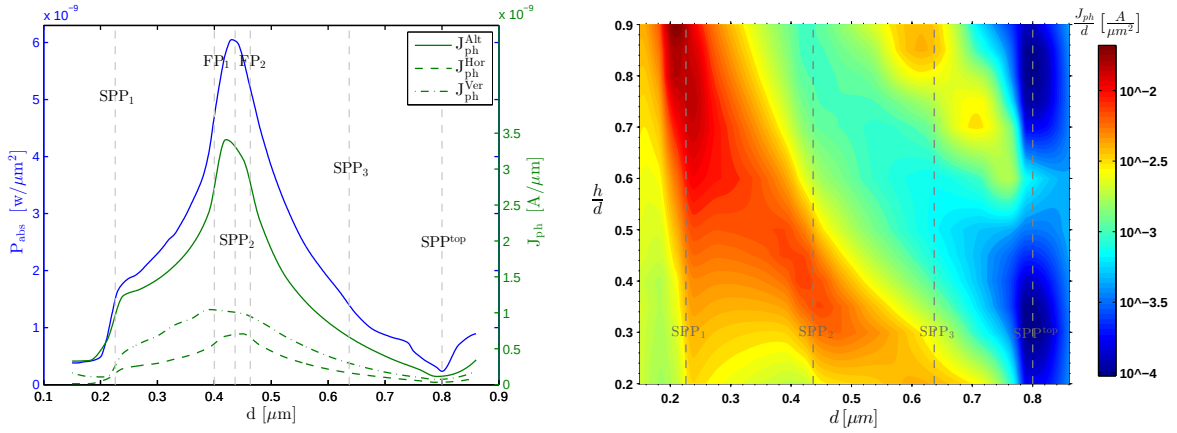

(a) (b)

Figure 3.5: a) Optical absorption and J_{AC} as defined for three types of bias as shown in Fig.3.4 $V_0 = 2V$, $w/d = 0.8$ and $h/d = 0.4$, incident power intensity of $0.1[W/cm^2]$, b) contour of (J_{AC}^{Alt}/d) with respect to d and h/d.

implies that higher spatial average optical absorption,$\bar{P}_{ave}$., leads to greater photocurrent for all bias configuration.

We also investigate the dependency of photocurrent to physical parameters of the photomixer. Fig. 3.6(a) shows that J_{DC}, which is mainly due to non-modulated portion of optical generation rate, increases with carrier lifetime of photoconductor, independent of terahertz frequency. However, AC component of the photocurrent drops for higher frequencies, and grows slightly with carrier lifetime of photoconductor [30]. Photocurrent variation with respect to bias voltage, V_0, is also presented in Fig. 3.6(b) for three bias types. Apparently, both AC and DC components of photocurrent increases with bias voltage, however it is limited by the break down field (around 5×10^5V/cm for LTG-GaAs) of the substrate.

3.5 Conclusion

Efficiency of a photoconductive source not only requires high absorbed power in photoconductor, but also depends on the high bias electric field at the point of carrier generation. In this paper, enhancement of optical power absorption by using resonance modes occurs

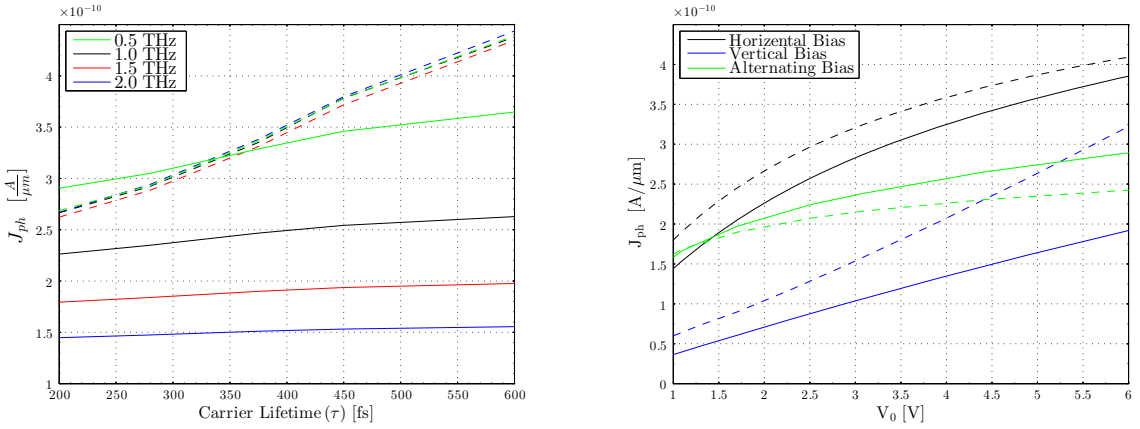

Figure 3.6: J_{AC} (solid lines) and J_{DC} (dashed lines) with respect to (a) bias voltage (V_0) for three types of bias configuration, (b) carrier lifetime of LTG-GaAs (from [**?**]) for alternating bias type. Optical intensity of beam is $0.1\,W/cm^2$.

in a one-dimensional metallic grating was studied. Then, the simulation results for the consequent generated photocurrents under three bias configurations are presented.

Chapter 4

Analysis of THz Waveguide

4.1 Introduction

THz photoconductive sources have been widely studied, and commonly used for scientific and commercial applications [4, 30]. Such sources are very versatile as they can be used for generating CW and pulsed THz radiation, and cover a wide range of frequency. These coherent sources can be designed such that the radiation be coupled directly into free-space [31] or into a waveguide for integrated applications [32]. In CW mode, the operation principle is based on the mixing of two CW lasers in a DC biased fast photoconductive material. Due to the photomixing, a CW photocurrent is generated with the beat frequency in THz range. In pulsed mode, however, the absorption of a single laser pulse in the photoconductor generates a transient pulse photocurrent. The resultant photocurrent in each case acts as the source of THz radiation.

Despite the good progress in optimizing the structure of such devices for improved performance [33], most of the proposed designs suffer from low optical-to-THz conversion efficiency. Enhancing the optical intensity in the regions where the DC bias field is maximized can increase the photocurrent and the THz signal substantially [11]. The conversion efficiency can be improved through careful manipulation of the THz signal for various applications [34]-[35]. It is therefore important to design a structure that enhances the optical intensity, and simultaneously guides or radiates the generated THz wave effectively. Thanks to the recent advancement in nano-technology fabrication techniques, implementation of plasmonic nano-structures with enhanced light localization has become feasible [36], [37].

In this paper, we propose a THz photmixing structure, based on the approach described in [37], that not only enhances the optical intensity in the active region through plasmonic modes but also guides generated THz signal. The structure is essentially a parallel plate waveguide (PPWG) with the top conducting plate replaced by a periodic array of sub-wavelength nano-slits. The substrate of the PPWG is made of a fast photoconductive material in which laser photomixing/absorption occurs. In Section II, the proposed structure is described. In Section III, the characteristic equation of the proposed waveguide is derived analytically, and its guided modes are studied in detail for THz range. The accuracy of the analytical results is verified against full-wave simulations for certain cases. Design consideration for THz photoconductive source application is also presented. In Section IV, based on dyadic Greens function representation, a systematic approach is provided for calculating the amplitude of the guided modes that are excited by an arbitrary photocurrent. Concluding remarks follow in Section V.

4.2 Description of Proposed Structure

The proposed guiding structure is illustrated in Fig. 4.1. It is based on grounded dielectric slab waveguide with a periodic array of sub-wavelength nano-strips loaded on the top of the dielectric. Metallic strips formed on the top have thickness t and separation width δ, and a periodicity Λ along y-axis. All aforementioned dimensions are assumed to be much smaller than THz wavelength ($t, \delta, \Lambda \ll \lambda_{THz}$). The bottom conductor plate is assumed to be uniform. The substrate has thickness h, and is made of a fast photoconductive material, such as low temperature grown GaAs (LTG-GaAs), with dielectric constant ϵ_r.

Since the width of the slits and strips are very small compared to THz wavelength, top plate can be effectively modelled as a uniform surface impedance sheet with anisotropic impedance boundary condition which has been vastly used for similar surfaces such as planar sheath helix [38]-[39]. These approximate boundary conditions state that on the top plate, the conductivity in the direction parallel to the strips is assumed very large whereas in perpendicular direction is assumed to be zero. As Shown in Fig. 4.1, the strip layer is illuminated from the free space by two laser beam with frequency difference equal to desired THz signal. Owing to the excitation of optical plasmonic modes, plasmon-assisted transmission occurs through the nano-slits at the designed wavelength [40], [41]. Enhanced optical field at the slits results in the high absorption rate of the optical photons and consequently large carrier generation rate. Generated carrier density is modulated with a THz frequency equal to difference between the frequencies of the two incident optical beams. This will generate a THz photocurrent, $\vec{J}_{ph}$, upon applying a DC bias field. Since,

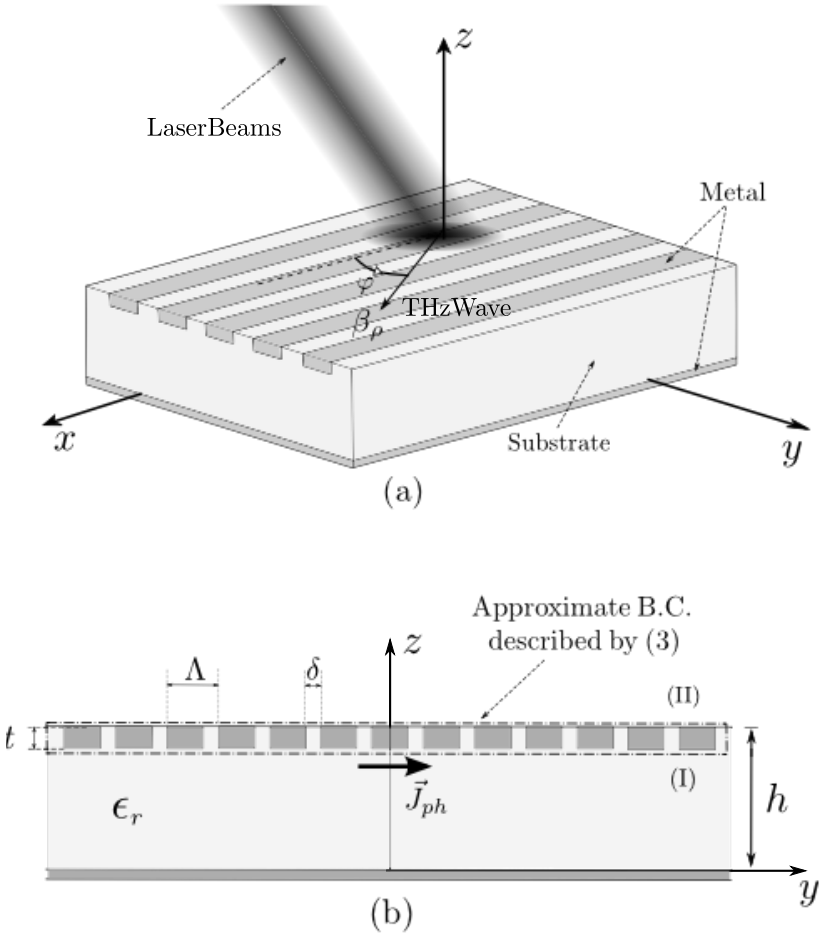

Figure 4.1: (a) 3D schematic of the proposed THz waveguide structure illuminated by two laser beam with frequency difference equal to desired THz signal. A THz guided mode propagating at an angle of φ with respect to x-axis is shown with a propagation constant of β_ρ, and (b) side view showing the physical parameters and a typical photocurrent vector. The strip layer is approximated by a boundary condition described by equation (4.3) in the text.

the amplitudes of excited THz modes are proportional to the projection of $\vec{J}_{ph}$ vector on the modal fields [19], and the direction of $\vec{J}_{ph}$ is mostly determined by the DC bias electric field [42], a certain desired THz mode can be excited by properly chosen configuration of electrodes ans their potential difference. In the following Section, a detailed discussion of

the guided modes supported by the proposed waveguide is presented.

4.3 THz Dispersion Characteristics of the Structure

Assuming that the propagation of THz wave occurs in an arbitrary direction (β_x, β_y) in xy plane, all field components have a (x, y) dependency of the form $e^{-j\beta_x x - j\beta_y y}$, where β_x and β_y are propagation constants along x and y directions, respectively. Electromagnetic fields in regions I and II can be represented as a superposition of TE- and TM-polarized modes with respect to y-coordinate. Therefore, z-dependency of the y-components of TM and TE fields can be expressed as,

$$E_y^{\mathrm{TM}}(z) = \begin{cases} e_1 \sin(\beta_z z), & 0 < z < h \\ e_2 \exp\left(-\alpha_z (z-h)\right), & h < z \end{cases} \tag{4.1a}$$

$$H_y^{\mathrm{TE}}(z) = \begin{cases} h_1 \cos(\beta_z z), & 0 < z < h \\ h_2 \exp\left(-\alpha_z (z-h)\right), & h < z \end{cases} \tag{4.1b}$$

where β_z and α_z are the phase constants in z direction for region (I) and (II), respectively, and e_1, h_1, e_2 and h_2 are constant field amplitudes. It should be noted that the perfect electric conductor (PEC) boundary condition is imposed on the field expression in (4.1) over the ground plane, at $z = 0$. Moreover, the relations between propagation constants in two regions are given by

$$(\mathrm{I}) : \beta_\rho^2 + \beta_z^2 = k_0^2 \epsilon_r, \qquad (\mathrm{II}) : \beta_\rho^2 - \alpha_z^2 = k_0^2 \tag{4.2}$$

where k_0 is the wave number in free space and β_ρ is the radial propagation constant in xy-plane defined as $\beta_\rho^2 = \beta_x^2 + \beta_y^2$. The approximate boundary conditions for a periodic strip sheet [43] at $z = h$ are

$$E_x^{\mathrm{I}} = E_x^{\mathrm{II}} = 0 \tag{4.3a}$$

$$E_y^{\mathrm{I}} = E_y^{\mathrm{II}} \tag{4.3b}$$

$$H_x^{\mathrm{I}} = H_x^{\mathrm{II}} \tag{4.3c}$$

Imposing the boundary conditions given in (4.3) on the field components derived from (4.1) leads to the dispersion relations for the guided modes. From (4.3a) one can derive

$$\omega \mu_0 \beta_z h_1 \sin(\beta_z h) = \beta_x \beta_y e_1 \sin(\beta_z h) \tag{4.4}$$

where μ_0 is vacuum permeability. A possible non-trivial solution of (4.4) is obtained when $\sin(\beta_z h) = 0$, provided that $\beta_x \beta_y \neq 0$. This results in the simplest type of modes, which are essentially parallel plate modes (PPMs) described by the following relation

$$\beta_\rho^2 = k_0^2 \epsilon_r - (m\pi/h)^2, \qquad m = 0, 1, 2, \ldots \tag{4.5}$$

The case $m = 0$ represents a z-polarized TEM mode with no variation with respect to z ($\beta_z = 0$). Discussion of two special cases of $\beta_x = 0$ or $\beta_y = 0$ will be presented in the following subsection.

For the other modes for which $\sin(\beta_z h) \neq 0$, the dispersion relation becomes

$$\tan(\beta_z h) = \frac{\alpha_z}{\beta_z} \frac{\beta_x^2 - k_0^2 \epsilon_r}{\beta_x^2 - k_0^2} \tag{4.6}$$

Propagation constants of the modes governed by (4.6) can be found by solving (4.2) and (4.6) simultaneously.

4.3.1 Properties of Guided Modes

Propagation in any arbitrary direction in xy-plane can be studied by simultaneously solving (4.2) and (4.6). It is assumed that the dielectric is lossless ($\mathrm{Im}\{\epsilon_r\} = 0$) and the modes are not radiating (α_z is a real number and $\alpha_z > 0$).

Since the propagation in the directions parallel and perpendicular to strips might be of the special interest, we examine these cases first. For the modes propagating along $\varphi = 0^\circ$ and $\varphi = 90^\circ$ directions, the dispersion relation given in (4.6) can be simplified to

$$\tan(\beta_z h) = -\frac{\beta_z}{\alpha_z}, \quad (\text{for } \varphi = 0^\circ) \tag{4.7a}$$

$$\tan(\beta_z h) = \epsilon_r \frac{\alpha_z}{\beta_z}, \quad (\text{for } \varphi = 90^\circ) \tag{4.7b}$$

where (4.7a) and (4.7b) are identical to the dispersion relation for TM and TE modes, respectively, of a grounded dielectric slab waveguide (GDSWG) with the substrate thickness h. Fig. **??** shows the dispersion diagram of the modes propagating parallel ($\varphi = 0^\circ$) and perpendicular ($\varphi = 90^\circ$) to strips versus a normalized frequency defined as $\kappa = 2k_0 h\sqrt{\epsilon_r - 1}/\pi$.

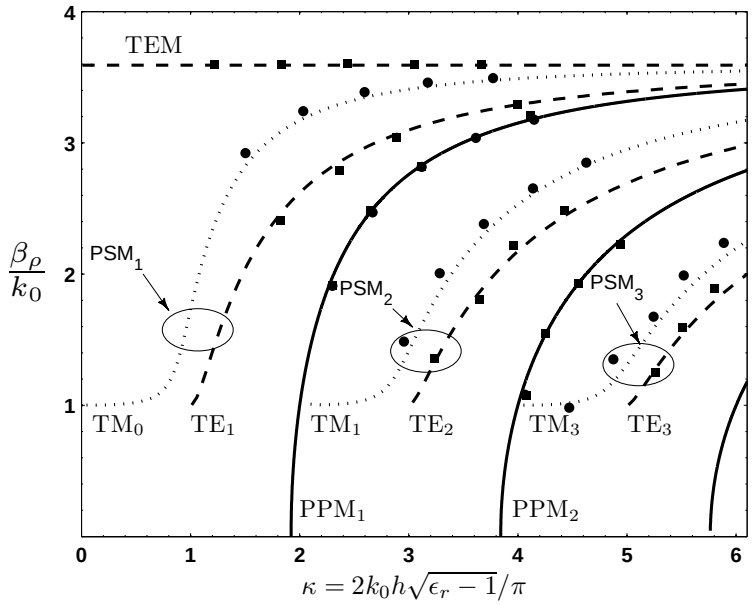

Figure 4.2: Dispersion diagram of the structure for modes propagating perpendicular and parallel to the strips. TEM mode and TE modes of GSWG (dashed line) propagate parallel to strips ($\varphi = 0$), whereas TM modes of GDSWG (doted line) propagate perpendicular to the strips ($\varphi = 90$). No TEM mode is supported at ($\varphi = 90$) direction. Parallel plate modes (PPM) (solid lines) exist for all φ directions. Square and circle markers are the results obtained from full wave simulation for parallel and perpendicular to strips, respectively.

From the above discussions, it should be clear that in addition to TE and TM modes of GDSWG that propagates parallel and perpendicular to the strips, respectively, a complete set of PPMs are supported by the structure in all directions [44] except for TEM mode propagating along $\varphi = 90°$ direction. However, the TEM mode can propagate along $\varphi = 0\,°$ direction because it satisfies (4.7a) when $\beta_z = 0$.

As a general case, we would like to study the propagation along an arbitrary φ direction as shown in Fig. 4.1. Therefore, each supported mode propagating with the propagation constant of β_ρ along φ direction and at the frequency of ω corresponds to a point on the dispersion surface $\omega = f(\beta_x, \beta_y)$. A 2-dimensional dispersion diagram of the non-radiating modes of the structure is shown in Fig. ??. The horizontal and vertical axis represents the normalized propagation constants along x- and y-axis, respectively, and the color scale is the normalized frequency, κ. The modes in Fig. ?? fall into two categories; perturbed

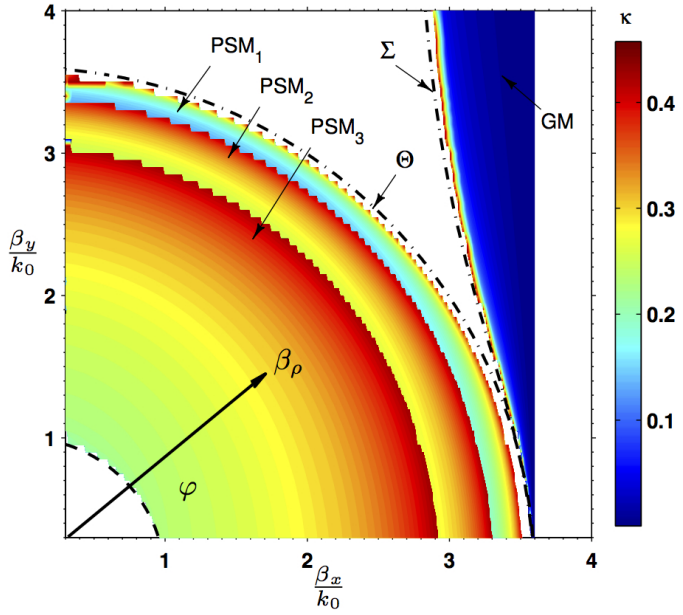

Figure 4.3: Contour diagram of dispersion surfaces $\omega = f(\beta_x, \beta_y)$ with normalized frequency, $\kappa = 2k_0h\sqrt{\epsilon_r - 1}/\pi$, for non-radiating modes propagating in xy-plane. Dispersion surfaces of all PSMs tend to extend to infinite frequency at $\beta_\rho/k_0 = \sqrt{\epsilon_r}$, but in this illustration their surfaces are truncated at $\kappa = 0.45$.

slab modes (PSMs) and grating modes (GMs). Dispersion surfaces for PSMs and GMs are inside and outside of the cylinder of $\beta_\rho/k_0 = \sqrt{\epsilon_r}$, respectively. The existence of GMs and PSMs has also been reported in [45] for a similar structure, and are referred to as grating modes, and surface wave modes, respectively. It is important to note that TE and TM modes of GDSWG shown in Fig. **??** are two cross sections of the dispersion surface of PSMs in Fig. **??** at $\beta_y = 0$ and $\beta_x = 0$, respectively. Furthermore, the TEM mode in Fig. **??** corresponds to a point where the dispersion surface of GM intersects with horizontal axis at $\beta_x/k_0 = \epsilon_r$. For all modes in Fig. **??**, the area inside the circle $\beta_\rho/k_0 = 1$ belongs to the radiating modes.

It is worth to note that the dispersion surface of all modes in Fig **??**, tends to extend to infinity at the vicinity of particular curves that are the locus of the poles of the spectral domain Green's function, which will be described in Section IV, at high frequencies [46], [47]. These "singularity curves" can be obtained by solving (4.2) and (4.6) in the limiting case of $k_0h \gg 1$. The locus of the singularity for PSMs and GM denoted by Θ and Σ

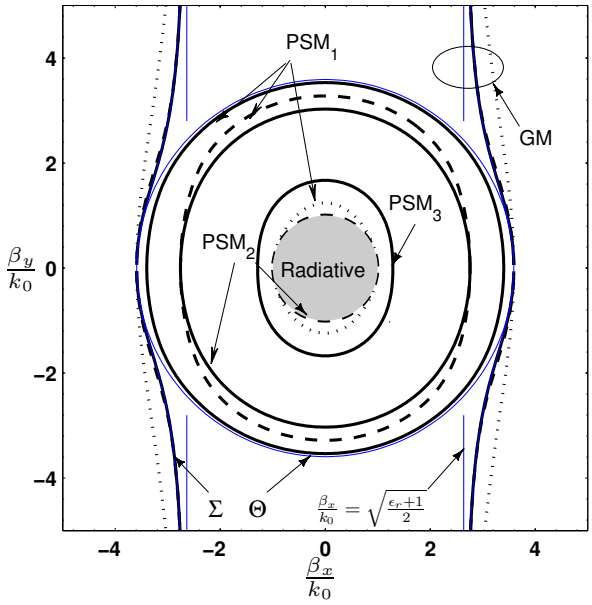

Figure 4.4: 2-dimension dispersion contours of PSMs and GMs for normalized frequencies, $\kappa = 5.3$ (Solid line), $\kappa = 2.3$ (dashed line), $\kappa = 0.8$ (dotted line). Circles $\beta_\rho/k_0 = 1$ and $\beta_\rho/k_0 = \sqrt{\epsilon_r}$ identify limiting cases of radiating and highly confined modes, respectively. $\beta_x = \pm k_0\sqrt{(\epsilon_r+1)/2}$ is asymptote of Σ when $\beta_y \to \infty$.

curves, respectively, are obtained as follows

$$\Theta(\beta_\rho) = \beta_\rho^2 - \epsilon_r\, k_0^2 = 0 \tag{4.8a}$$

$$\Sigma(\beta_\rho) = \beta_\rho^4 \cos^2\varphi - \beta_\rho^2 k_0^2(\cos^2\varphi + 1)\frac{\epsilon_r+1}{2} + k_0^4\epsilon_r = 0 \tag{4.8b}$$

which are a circle and hyperbola in (β_x^2, β_y^2) plane, respectively. $\Sigma = 0$ plot has an asymptote of the form $\frac{\beta_x}{k_0} = \sqrt{(\epsilon_r+1)/2}$ in (β_x, β_y) plane [46], when $\beta_y \to \infty$. Therefore, GMs can only propagate parallel to the strips with propagation constant limited to the interval $k_0\sqrt{(\epsilon_r+1)/2} \le \beta_x \le k_0\sqrt{\epsilon_r}$, which corresponds to the propagation constants of the symmetrical mode of a slot line [48] and of the TEM mode of a parallel plate waveguide, respectively.

To gain more insight into dispersion surfaces of Fig. ??, constant frequency contours corresponding to PSMs and GMs for different values of κ are plotted in Fig. **??**. All PSM contours are inside $\Theta = 0$ circle that is singularity curve of dispersion surfaces, and outside of $\beta_\rho/k_0 = 1$ circle, which contains all the radiating modes. Thus, the modes outside the $\beta_\rho/k_0 = 1$ disk are more confined (non-radiating) in the substrate. As shown in Fig. **??**, the constant frequency contours are not perfect circles, rather elongated along y-axis. When the normalized frequency increases, the contours approach the dispersion surface singularity circle of $\beta_\rho/k_0 = \sqrt{\epsilon_r}$. On the other hand, when normalized frequency decreases to cut-off frequency of TE and TM modes of GDSWG, the contours become tangential to $\beta_\rho/k_0 = 1$ circle.

It should be emphasized that PSMs are identical to TE modes of GDSWG at $\varphi = 0°$, and gradually transform to TM modes of GDSWG as the the propagation angle increases to $\varphi = 90°$. This is why in Fig. **??**, TM_m and TE_{m+1} $(m = 0, 1, ...)$ are grouped as PSM_{m+1}. Besides, TM_m and TE_{m+1} modes of GDSWG have normalized cut-off frequencies at $\kappa = 2m$ and $\kappa = 2m + 1$, respectively, as shown in Fig. **??**. Thus, by normalizing the operating frequency, the propagating PSM modes are easily determined. It is interesting to note that when the normalized frequency is between the normalized cut-off frequencies of a TE and TM mode of the same PSM group. That PSM mode is a guided mode if the propagation angle is beyond a certain value $(\varphi_0 \leq \varphi \leq 90°)$. The same mode becomes radiative when $0 \leq \varphi \leq \varphi_0$. For example, in Fig. **??** consider the PSM_1 for $\kappa = 0.8$ which is below the cut-off of TE_1 (radiating mode) and above the cut-off of TM_0 (guiding mode). As seen in Fig. **??**, its contour is out of the radiative circle for propagation angles around $\varphi = 90°$ and is tangent to the radiative circle for propagation angles around $\varphi = 0$. Although there is no abrupt transition between the radiative and guided modes with respect to propagation angle, but this property of the structure might be suitable for some applications, such as beam steering.

4.3.2 Comparisons with Other Methods

Metal strip grating on a grounded slab has been widely studied in the literature. For example, using more complex Sakurai-Vainshtein-Sivov boundary conditions, structures with small substrate thickness ($k_0 h \ll 1$) has been analysed for various strip densities (δ/Λ) [45]. It should be mentioned that the dispersion relation in (4.6) is identical to Eq. (32) of [45]. This verifies the validity of the simple anisotropic conductivity boundary condition used here. Moreover, in [49] such a structure has been studied by the method of moment in spectral domain for negligible thickness of strips, but with a period comparable with the wavelength. In [45] and [49], the normalized phase constant of the GM is reported

Table 4.1: Comparison between theoretical and simulation results for guided modes

φ	β_ρ/k_0	Mode	Method	k_0h	β_z/k_0	α_z/k_0
0°	0.06	PSM_3	Theory	2.39	0.04	0.17
			FEM	2.33	0.05	0.16
30°	3.79	GM	Theory	0.81	$j1.21$	3.71
			FEM	0.80	$j1.06$	3.66
30°	2.54	PSM_1	Theory	0.81	0.10	0.09
			FEM	0.79	0.10	0.10
75°	10.31	GM	Theory	2.51	$j9.67$	10.26
			FEM	2.44	$j8.60$	15.60
90°	0.10	PSM_2	Theory	1.37	0.23	0.08
			FEM	1.31	0.21	0.10

as a function of the propagation angle only at single frequency as opposed to a frequency range reported here.

In order to verify the accuracy of the analytical results, the proposed waveguide structure in Fig. 4.1 was simulated by Ansoft HFSS, a full-wave EM solver based on finite element method (FEM). In the simulated model, the metallic parts was chosen to be gold with geometrical parameters $\Lambda = 400$ nm, $t = 100$ nm and $\delta = 100$ nm. The propagation constants for $\varphi = 0°$ and $\varphi = 90°$ obtained from full-wave simulation are mapped onto the dispersion diagrams in Fig. **??**. For further comparison, the frequency and the wave numbers in transverse direction obtained from full-wave simulation and the analytical method for different modes and propagation angles are reported in Table I showing an excellent agreement between the two methods.

4.3.3 Design Considerations for THz Photoconductive Source Application

It is important to note that in a practical and realizable structure, the substrate thickness is of the order of THz wavelength. Therefore, in contrary to lower frequency assumption where $k_0h \ll 1$, in the proposed application for operation around 1 THz, one would have $k_0h \sim 5$. Thus, for such relatively thick substrate made of typical photoconductors, one

would have $\kappa \sim 10$. For such a large κ, the dispersion contours become closer to the asymptotes of the dispersion surfaces, and thus the poles of the spectral domain Green's function corresponding to the fundamental modes of PSM_1 and GM lie on Σ and Θ curves defined in (4.8). This can be considered as an advantage as the asymptotic behavior of the dispersion surfaces provide extremely low-dispersion guided modes because the normalized propagation constant becomes almost independent of frequency for large κ (see Fig. **??**). The Green's function will be described in the following Section.

Basically, for sufficiently thick substrate, the effect of the substrate ground plane on GM propagation is minimal. Furthermore, due to short optical absorption length of LTG-GaAs ($\sim 1\,\mu m$), the generated photocurrent is mostly localized at the vicinity of the strips, and its direction can be dominantly set in y-direction by e.g. applying an incrementally increasing bias voltage between strips. Since x- and y-polarized electric field of PPMs vanish at the strips layer, these modes cannot be excited by a photocurrent located at $z = h$. However, low order PSMs and GM demonstrate strong y-polarized field at $z = h$. The field distribution of the PSM_1 and GM are plotted in Fig. 4.5 for two propagation angles of $\varphi = 30°$ and $\varphi = 60°$. As observed in contour diagram of Fig. **??**, for large values of κ, PSM_1 has almost φ-symmetric distribution and propagates away from the source almost isotropically. On the other hand, confinement of the GM field around $z = h$ for propagation angles around $\varphi = 90°$ is significantly more than that for $\varphi = 0°$. Therefore, this mode is the most desired in integrated THz wave-guiding applications.

4.4 Excitation of the THz Modes by a Photocurrent Dyadic

Green's function ($\mathbf{G}$) approach [46], [50] can be used to find the guided modes of the structure excited by an arbitrary photocurrent source. Those components of $\mathbf{G}$ that correspond to a current source along the x-coordinate is not of interest here, because of very small projection of modal fields along the strips, as shown in Fig. (4.5). Moreover, producing the z-oriented photocurrent is not practical due to the large thickness of substrate in terms of the optical absorption length of LTG-GaAs. Thus, only significant components of dyadic Green's function for the current element, $\vec{J} = \hat{y}\,\delta(x)\,\delta(y)\,\delta(z - h^{-})$, are of interest in this analysis. Spectral electric field Green's function of the structure shown in Fig. 4.1(b) in the free space region above the substrate, can be derived as described in [46]

$$\begin{pmatrix} \tilde{G}_{yz} \\ \tilde{G}_{yy} \end{pmatrix} = \begin{pmatrix} \frac{\beta_y}{\alpha_z} \\ -j \end{pmatrix} \frac{\omega\mu_0 e^{-\alpha_z(z-h)}}{\cot(\beta_z h)(k_0^2\epsilon_r - \beta_x^2)/\beta_z - (k_0^2 - \beta_x^2)/\alpha_z} \tag{4.9}$$

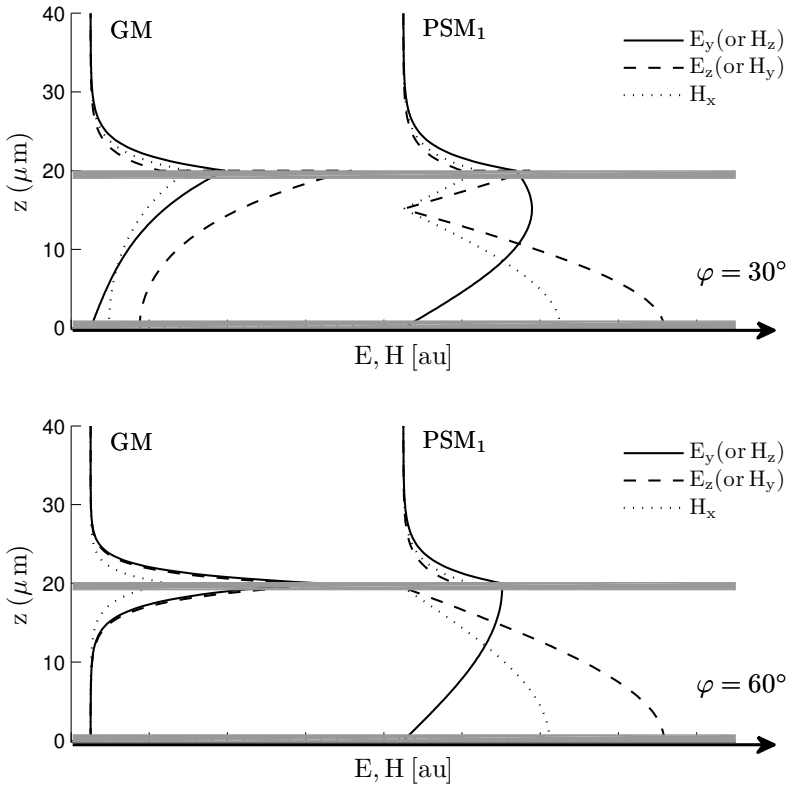

Figure 4.5: GM and PSM_1 normalized field distribution of $\vec{E}$ and $\eta_0\vec{H}$, (where $\eta_0 = \sqrt{\mu_0/\epsilon_0}$) with respect to z for typical values of $\kappa = 5.3$ and $h = 20$ when the waves are propagating along $\varphi = 30°$ (top) and $\varphi = 60°$(bottom). In both sets of modes, E_x is zero and H_z and H_y are proportional to E_y and E_z, respectively

where β_z and α_z are defined by (4.2) and equating the denominator in (4.9) to zero will lead to the characteristic equation (4.6). It should be noted that (4.3a) and reciprocity of electromagnetic field result in $\tilde{G}_{yx} = 0$ for such a current source. Inverse Fourier transform (FT) of each component of dyadic Green's function corresponding to a source located at $(0, 0, h^-)$ is expressed by

$$\mathbf{G}(x,y,z|0,0,h^{\text{-}}) = \int_{-\infty}^{+\infty}\int_{-\infty}^{+\infty} \tilde{\mathbf{G}}(\beta_x,\beta_y,z) e^{j\beta_x x + j\beta_y y}\,\mathrm{d}\beta_x\,\mathrm{d}\beta_y \tag{4.10}$$

where $(x,y,z) = (\rho\cos\phi, \rho\sin\phi, z)$ are coordinates of the observation point, and $(\beta_x,\beta_y) = (\beta_\rho\cos\varphi, \beta_\rho\sin\varphi)$ are spectral domain coordinates. Numerical calculation of (4.10) whose integrand is extremely oscillatory is very cumbersome. Hence, to calculate the integral of (4.10) we follow an asymptotic approach, which has been widely used for similar structures in the past [51],[52].

Inverse Fourier transform of Green Function, corresponding to (**??**), in cylindrical coordinate system is expressed by

$$G(x,y,z|z') = \frac{1}{4\pi^2}\int_0^{2\pi}\int_0^{\infty} \tilde{G}(\beta_x,\beta_y,z|z') e^{j\vec{\beta_\rho}\cdot\vec{\rho}}\,\beta_\rho\,\mathrm{d}\beta_\rho\,\mathrm{d}\varphi \tag{4.11}$$

Symmetry of the structure imposes $\tilde{G}(\varphi+\pi) = \pm\tilde{G}(\varphi)$ and $\tilde{G}(-\varphi) = \pm\tilde{G}(\varphi)$ on any component of dyadic green's function(upper or lower signs), Which the former indicate even or oddness of $\tilde{G}$ and latter indicates periodicity of π of $\tilde{G}$. Thus its Fourier series of $\tilde{G}$ for upper and lower signs is given by

$$\tilde{G}(\beta_\rho\cos\varphi,\beta_\rho\sin\varphi,z|z') = \sum_{n=0}^{\infty}\tilde{g}_n(\beta_\rho,z|z')\begin{pmatrix}\cos 2n\varphi\\ \sin(2n+1)\varphi\end{pmatrix} \tag{4.12}$$

Substituting (4.12) in (4.13) yields

$$\begin{aligned} G(x,y,z|z') = &\frac{1}{4\pi^2}\int_0^{\infty}\beta_\rho\,\mathrm{d}\beta_\rho\times \\ &\sum_{n=0}^{\infty}\tilde{g}_n(\beta_\rho,z|z')\int_0^{\pi} e^{j\beta_\rho\rho\cos(\varphi-\theta)}\begin{pmatrix}\cos 2n\varphi\\ \sin(2n+1)\varphi\end{pmatrix}\mathrm{d}\varphi \end{aligned} \tag{4.13}$$

From [53] eq. 9.1.21 we have:

$$\int_0^{\pi} \mathrm{d}\varphi e^{j\beta_\rho \rho \cos(\theta-\varphi)} \begin{pmatrix} \cos\ 2n\varphi \\ \sin\,(2n+1)\varphi \end{pmatrix} = \pi(-1)^n \begin{pmatrix} J_{2n}(\beta_\rho\rho)\cos\ 2n\theta \\ jJ_{2n+1}(\beta_\rho\rho)\sin\,(2n+1)\theta \end{pmatrix} \tag{4.14}$$

Moreover, by letting $\beta_\rho = \beta'_\rho e^{i\pi}$, and using $J_n(x) = 1/2\,[H_n^{(1)}(x) + H_n^{(2)}(x)]$ and the reflection formulas of Hankel function $H_n^{(1)}(e^{i\pi}x) = -(-1)^n H_n^{(2)}(x)$, and considering the fact that $\tilde{g}_n(\beta_\rho, z|z')$ is even (or odd) function of β_ρ if $\tilde{G}$ is even (or odd), we obtain

$$G(x,y,z|z') = \frac{1}{4\pi}\sum_{n=0}^{\infty}(-1)^n \begin{pmatrix} \cos\ 2n\theta \\ \sin\,(2n+1)\theta \end{pmatrix} \times \int_{-\infty e^{i\pi}}^{+\infty} \beta_\rho\,\mathrm{d}\beta_\rho \tilde{g}_n(\beta_\rho, z|z') \begin{pmatrix} H_{2n}^{(2)}(\beta_\rho\rho) \\ jH_{2n+1}^{(2)}(\beta_\rho\rho) \end{pmatrix} \tag{4.15}$$

where the integration contour has been changed to Sommerfeld path (C_1).Choosing the branch-cut along negative real axis for all orders of $H_n^{(1)}(x)$ [54], the large-argument formula of Hankel function, $H_n^{(2)}(x) \to \sqrt{\frac{2}{j\pi x}} j^{-n} e^{-jx}$ leads to

$$G(x,y,z|z') = \sqrt{\frac{1}{j8\pi\rho}} \times \int_{-\infty e^{i\pi}}^{+\infty} \tilde{G}(\beta_\rho\cos\theta, \beta_\rho \sin\theta, z|z')\sqrt{\beta_\rho} e^{-j\beta_\rho\rho}\,\mathrm{d}\beta_\rho \tag{4.16}$$

Ultimately, electric field at air region can be obtained by

$$\vec{\mathrm{E}}(x,y,z) = \sqrt{\frac{1}{j8\pi\rho}} \times \int_{-\infty e^{i\pi}}^{+\infty} \sqrt{\beta_\rho}\,\tilde{\mathbf{G}}(\beta_\rho\cos\phi, \beta_\rho\sin\phi, z).\vec{\tilde{J}}_{ph} e^{-j\beta_\rho\rho}\,\mathrm{d}\beta_\rho \tag{4.17}$$

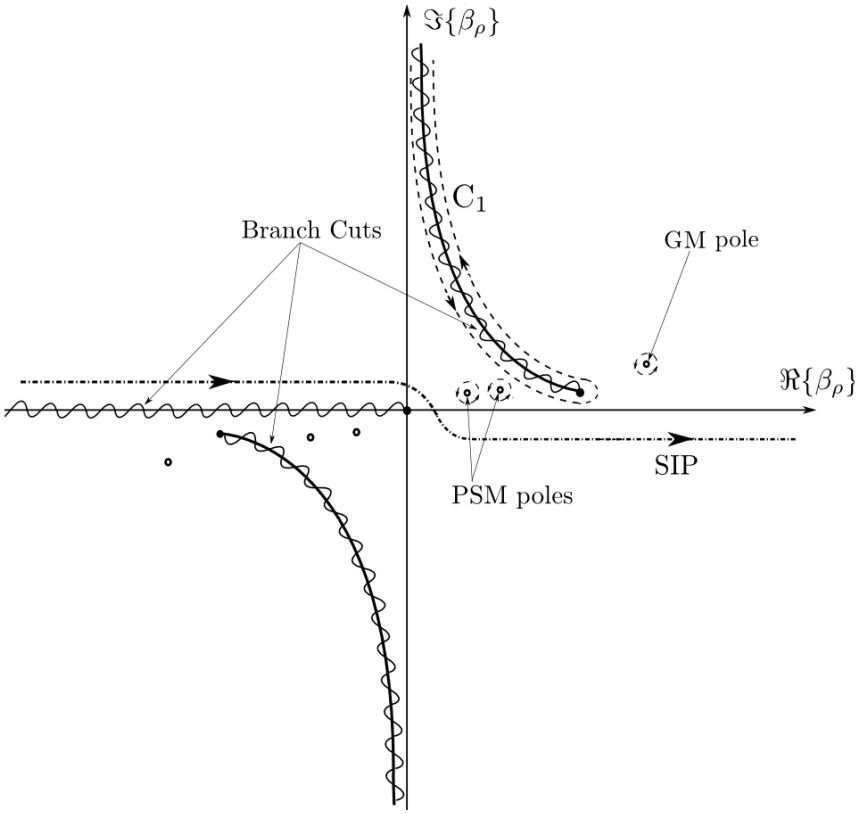

Figure 4.6: Contour integration on complex plane of β_ρ. SIP is deformed to give an integral over C_1 plus the summation of the residue of the enclosed poles.

where $\vec{\tilde{J}}_{ph}$ is the Fourier transform of the photocurrent vector. Eq. (4.17) can be interpreted as a summation of cylindrical waves departing the source and weighted by the product of spectral domain Green's function and Fourier transform of the photocurrent distribution. Furthermore, the main contribution to the field at a point in far-field comes from the modes propagating exactly toward that point, and the impact of the modes propagating in other directions is vanished at far-field due to destructive interferences.

Integration in (4.17) is taken on a regular Sommerfeld integration path (SIP), where the branch-cuts are illustrated in Fig. 4.6. Besides, a small loss is introduced to move the branch points away from real axis in β_ρ plane. Integration path can be deformed to C_1. The sum of the residues of the enclosed poles in the upper half-plane should now be added to the integration around the branch-cut. The summation represents guided modes generated by the photo-current and the integral represents the continuous spectrum of the

radiating modes [52]. The expression in (11) may be rewritten as,

$$\vec{\mathrm{E}}(x,y,z) = \sqrt{\frac{1}{j8\pi\rho}}\left[\sum_n 2\pi j R_{\beta_{\rho n}} e^{-j\beta_{\rho n}\rho} + \int_{C_1} \sqrt{\beta_\rho}\,\tilde{\mathbf{G}}(\beta_\rho\cos\phi, \beta_\rho\sin\phi, z).\vec{\tilde{J}}_{ph} e^{-j\beta_\rho\rho}\,\mathrm{d}\beta_\rho\right] \tag{4.18}$$

where the residue, $R_{\beta_{\rho n}}$, corresponds to nth pole ($\beta_{\rho n}$) of the integrand in (4.17) and can be found as

$$R_{\beta_{\rho n}} = \lim_{\beta_\rho \to \beta_{\rho n}} (\beta_\rho - \beta_{\rho n})\sqrt{\beta_\rho}\,\tilde{\mathbf{G}}.\vec{\tilde{J}}_{ph} \tag{4.19}$$

It is evident that by substituting (4.9) in (4.19), the terms of the summation in (4.18) will have spatial forms identical to those of modal fields in (4.1). Although (4.18) can be applied to any arbitrary current distribution, as an example, we assume that $\vec{\tilde{J}}_{ph}$ is an infinitesimally small current element in y-direction as shown in Fig. 4.1. This current element can be created by focusing laser beams that are incident normal to the top surface, and by applying an incrementally increasing DC bias between the strips. In such case, one can obtain the residue for E_y for the case where $\vec{\tilde{J}}_{ph} = 1\hat{y}$ for the first order GM pole as

$$R_{\beta_{\rho 0}} = \omega\mu_0 \frac{\alpha_{z0}\beta_{z0}\sqrt{\beta_{\rho 0}}}{\Sigma'(\beta_{\rho 0})} e^{-\alpha_{z0}(z-h)} \tag{4.20}$$

where all 0 subscripts represents the values at GM pole and $\Sigma' = \frac{\mathrm{d}\Sigma}{\mathrm{d}\beta_\rho}$. It can be easily shown that this residue increases as φ increases from 0° to 90°, so such current element is coupled strongly to the modes propagating perpendicular to the strips. The same steps might be taken to find the amplitudes of the PSM modes. The calculated amplitudes of the GM and PSMs excited by a y-oriented current element at $z' = h^-$ for $\kappa = 5.3$, as a function of propagation direction are plotted in Fig. 4.7. As explained in the previous Section and shown in Fig. 4.7, GM propagation pattern is highly directive and tends to infinity at $\varphi = 90°$. As shown in Fig. 4.7, PSMs are also excited by the same current element, but with much smaller amplitude as compared to GM. This is in agreement with Fig. 12 of [46].

4.5 Conclusion

A complete analysis of the proposed structure as a THz photo-mixer source involves two problems; photo-mixing and photo-current generation problem and the problem of THz

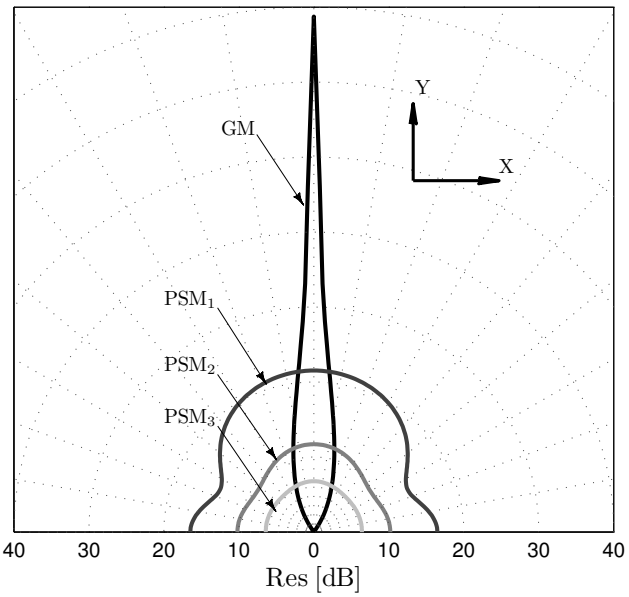

Figure 4.7: Coupling coefficient of the GM and PSMs excited by a current element at $z' = h^-$ for $\kappa = 5.3$.

wave excitation and guidance/radiation due to the generated photo-current. In this paper, the latter problem was addressed in detail. A fast and accurate modal analysis was presented along with the THz excitation due to an arbitrary photo-current. The proposed structure is a suitable candidate for high efficient THz generation in integrated microsystem applications.

References

[1] JA Porto, FJ Garcia-Vidal, and JB Pendry. Transmission resonances on metallic gratings with very narrow slits. *Physical review letters*, 83(14):2845–2848, 1999.

[2] P.H. Siegel. Terahertz technology. *Microwave Theory and Techniques, IEEE Transactions on*, 50(3):910–928, 2002.

[3] GP Gallerano, S. Biedron, et al. Overview of terahertz radiation sources. In *Proceedings of the 2004 FEL Conference*, pages 216–221, 2004.

[4] D. Saeedkia and S. Safavi-Naeini. Terahertz photonics: Optoelectronic techniques for generation and detection of terahertz waves. *Lightwave Technology, Journal of*, 26(15):2409–2423, 2008.

[5] H. Engan. Excitation of elastic surface waves by spatial harmonics of interdigital transducers. *Electron Devices, IEEE Transactions on*, 16(12):1014–1017, 1969.

[6] T.W. Ebbesen, HJ Lezec, HF Ghaemi, T. Thio, and PA Wolff. Extraordinary optical transmission through sub-wavelength hole arrays. *Nature*, 391(6668):667–669, 1998.

[7] D. Crouse and P. Keshavareddy. A method for designing electromagnetic resonance enhanced silicon-on-insulator metal–semiconductor–metal photodetectors. *Journal of Optics A: Pure and Applied Optics*, 8(2):175, 2006.

[8] S.H. Kim, C.M. Lee, S.B. Sim, W.S. Han, K.J. Ahn, K.J. Yee, et al. Enhanced in and out-coupling of ingaas slab waveguides by periodic metal slit arrays. *Optics Express*, 20(6):6365–6374, 2012.

[9] C.W. Berry, M.R. Hashemi, M. Unlu, and M. Jarrahi. Significant radiation enhancement in photoconductive terahertz emitters by incorporating plasmonic contact electrodes. *arXiv preprint arXiv:1209.1680*, 2012.

[10] B. Heshmat, H. Pahlevaninezhad, Y. Pang, M.M. Shirazi, R.B. Lewis, T. Tiedje, R. Gordon, and T.E. Darcie. Nanoplasmonic terahertz photoconductive switch on gaas. *Nano Letters*, 2012.

[11] S.G. Park, K.H. Jin, M. Yi, J.C. Ye, J. Ahn, and K.H. Jeong. Enhancement of terahertz pulse emission by optical nanoantenna. *ACS nano*, 6(3):2026–2031, 2012.

[12] S.G. Park, Y. Choi, Y.J. Oh, and K.H. Jeong. Terahertz photoconductive antenna with metal nanoislands. *Optics Express*, 20(23):25530–25535, 2012.

[13] S. Jafarlou, M. Neshat, and S. Safavi-Naeini. A fast method for analysis of guided waves and radiation from a nano-scale slit loaded waveguide for a thz photoconductive source.

[14] P. Zilio, D. Sammito, G. Zacco, and F. Romanato. Absorption profile modulation by means of 1d digital plasmonic gratings. *Optics Express*, 18(19):19558–19565, 2010.

[15] C. Min, J. Li, G. Veronis, J.Y. Lee, S. Fan, and P. Peumans. Enhancement of optical absorption in thin-film organic solar cells through the excitation of plasmonic modes in metallic gratings. *Applied Physics Letters*, 96(13):133302–133302, 2010.

[16] VN Truchin, AV Andrianov, and NN Zinovev. Generation of terahertz radiation by a moving bunch of nonequilibrium electron-hole plasma. *Physical Review B*, 78(15):155325, 2008.

[17] P.U. Jepsen, RH Jacobsen, and SR Keiding. Generation and detection of terahertz pulses from biased semiconductor antennas. *JOSA B*, 13(11):2424–2436, 1996.

[18] T. Dekorsy, T. Pfeifer, W. Kütt, and H. Kurz. Subpicosecond carrier transport in gaas surface-space-charge fields. *Physical Review B*, 47(7):3842, 1993.

[19] M. Neshat, D. Saeedkia, L. Rezaee, and S. Safavi-Naeini. A global approach for modeling and analysis of edge-coupled traveling-wave terahertz photoconductive sources. *Microwave Theory and Techniques, IEEE Transactions on*, 58(7):1952–1966, 2010.

[20] P. Sheng, RS Stepleman, and PN Sanda. Exact eigenfunctions for square-wave gratings: Application to diffraction and surface-plasmon calculations. *Physical Review B*, 26(6):2907, 1982.

[21] P. Lalanne, JP Hugonin, S. Astilean, M. Palamaru, and KD Möller. One-mode model and airy-like formulae for one-dimensional metallic gratings. *Journal of Optics A: Pure and Applied Optics*, 2(1):48, 1999.

[22] R. Gordon and A.G. Brolo. Increased cut-off wavelength for a subwavelength hole in a real metal. *Opt. Express*, 13(6):1933–1938, 2005.

[23] ATM Rahman, K. Vasilev, and P. Majewski. Analytical solution of the fundamental waveguide mode of one-dimensional transmission grating for tm polarization. *JOSA B*, 28(12):2919–2924, 2011.

[24] A.D. Rakic, A.B. Djurišic, J.M. Elazar, and M.L. Majewski. Optical properties of metallic films for vertical-cavity optoelectronic devices. *Applied Optics*, 37(22):5271–5283, 1998.

[25] E.D. Palik. *Handbook of optical constants of solids*, volume 3. Academic press, 1998.

[26] M.G. Deceglie, V.E. Ferry, A.P. Alivisatos, and H.A. Atwater. Design of nanostructured solar cells using coupled optical and electrical modeling. *Nano letters*, 12(6):2894–2900, 2012.

[27] S.L. Chuang. *Physics of optoelectronic devices (Series in pure & applied optics)*. New York: Wiley, 2009.

[28] H. Nemec, A. Pashkin, P. Kuzel, M. Khazan, S. Schnull, and I. Wilke. Carrier dynamics in low-temperature grown gaas studied by terahertz emission spectroscopy. *Journal of Applied Physics*, 90(3):1303–1306, 2001.

[29] C. Canali, G. Majni, R. Minder, and G. Ottaviani. Electron and hole drift velocity measurements in silicon and their empirical relation to electric field and temperature. *Electron Devices, IEEE Transactions on*, 22(11):1045–1047, 1975.

[30] S. Preu, GH Döhler, S. Malzer, LJ Wang, and AC Gossard. Tunable, continuous-wave terahertz photomixer sources and applications. *Journal of Applied Physics*, 109:061301, 2011.

[31] KA McIntosh, ER Brown, KB Nichols, OB McMahon, WF DiNatale, and TM Lyszczarz. Terahertz measurements of resonant planar antennas coupled to low-temperature-grown gaas photomixers. *Applied physics letters*, 69(24):3632–3634, 1996.

[32] E.A. Michael. Travelling-wave photonic mixers for increased continuous-wave power beyond 1 thz. *Semiconductor science and technology*, 20(7):S164, 2005.

[33] I.S. Gregory, C. Baker, W.R. Tribe, I.V. Bradley, M.J. Evans, E.H. Linfield, A.G. Davies, and M. Missous. Optimization of photomixers and antennas for continuous-wave terahertz emission. *Quantum Electronics, IEEE Journal of*, 41(5):717–728, 2005.

[34] A. Novitsky, M. Zalkovskij, R. Malureanu, and A. Lavrinenko. Microscopic model of the thz field enhancement in a metal nanoslit. *Optics Communications*, 284(23):5495–5500, 2011.

[35] MA Seo, HR Park, SM Koo, DJ Park, JH Kang, OK Suwal, SS Choi, PCM Planken, GS Park, NK Park, et al. Terahertz field enhancement by a metallic nano slit operating beyond the skin-depth limit. *Nature Photonics*, 3(3):152–156, 2009.

[36] H. Tanoto, JH Teng, QY Wu, M. Sun, ZN Chen, SA Maier, B. Wang, CC Chum, GY Si, AJ Danner, et al. Greatly enhanced continuous-wave terahertz emission by nano-electrodes in a photoconductive photomixer. *Nature Photonics*, 6(2):121–126, 2012.

[37] B.Y. Hsieh and M. Jarrahi. Analysis of periodic metallic nano-slits for efficient interaction of terahertz and optical waves at nano-scale dimensions. *Journal of Applied Physics*, 109(8):084326–084326, 2011.

[38] MF Pasik and DG Dudley. An asymptotic analysis of a wire mesh parallel-plate waveguide. *Radio science*, 29(3):561–576, 1994.

[39] R. Arora. Surface waves on a pair of parallel undirectionally conducting screens. *Antennas and Propagation, IEEE Transactions on*, 14(6):795–797, 1966.

[40] S. Collin, F. Pardo, R. Teissier, and J.L. Pelouard. Efficient light absorption in metal–semiconductor–metal nanostructures. *Applied physics letters*, 85(2):194–196, 2004.

[41] S.B. Eryilmaz, O. Tidin, and A.K. Okyay. Plasmonic nanoslit array enhanced metal–semiconductor–metal optical detectors. *Photonics Technology Letters, IEEE*, 24(7):548–550, 2012.

[42] D. Saeedkia, R.R. Mansour, and S. Safavi-Naeini. The interaction of laser and photoconductor in a continuous-wave terahertz photomixer. *Quantum Electronics, IEEE Journal of*, 41(9):1188–1196, 2005.

[43] A.A. Kishk and P.S. Kildal. Asymptotic boundary conditions for strip-loaded surfaces of cylindrical structures with arbitrarily shaped cross-section. In *Antennas and Propagation Society International Symposium, 1999. IEEE*, volume 2, pages 834–837. IEEE, 1999.

[44] P. Burghignoli, P. Baccarelli, F. Frezza, A. Galli, P. Lampariello, and A.A. Oliner. Low-frequency dispersion features of a new complex mode for a periodic strip grating

on a grounded dielectric slab. *Microwave Theory and Techniques, IEEE Transactions on*, 49(12):2197–2205, 2001.

[45] FH Bellamine and E.F. Kuester. Guided waves along a metal grating on the surface of a grounded dielectric slab. *Microwave Theory and Techniques, IEEE Transactions on*, 42(7):1190–1197, 1994.

[46] Z. Sipus, H. Merkel, and P.S. Kildal. Green's functions for planar soft and hard surfaces derived by asymptotic boundary conditions. In *Microwaves, Antennas and Propagation, IEE Proceedings*, volume 144, pages 321–328. IET, 1997.

[47] N.K. Das and A. Mohanty. Infinite array of printed dipoles integrated with a printed strip grating for suppression of cross-polar radiation. i. rigorous analysis. *Antennas and Propagation, IEEE Transactions on*, 45(6):960–972, 1997.

[48] S.B. Cohn. Slot line on a dielectric substrate. *Microwave Theory and Techniques, IEEE Transactions on*, 17(10):768–778, 1969.

[49] P. Baccarelli, P. Burghignoli, F. Frezza, A. Galli, P. Lampariello, G. Lovat, and S. Paulotto. Modal properties of surface and leaky waves propagating at arbitrary angles along a metal strip grating on a grounded slab. *Antennas and Propagation, IEEE Transactions on*, 53(1):36–46, 2005.

[50] Z. Sipus, P.S. Kildal, and J. Salmonsson. Two-dimensional analysis of bandwidth of open hard surface. In *Microwaves, Antennas and Propagation, IEE Proceedings*, volume 143, pages 475–481. IET, 1996.

[51] P. Baccarelli, P. Burghignoli, F. Frezza, A. Galli, G. Lovat, and D.R. Jackson. Uniform analytical representation of the continuous spectrum excited by dipole sources in a multilayer dielectric structure through weighted cylindrical leaky waves. *Antennas and Propagation, IEEE Transactions on*, 52(3):653–665, 2004.

[52] M. Marin, S. Barkeshli, and P.H. Pathak. Efficient analysis of planar microstrip geometries using a closed-form asymptotic representation of the grounded dielectric slab green's function. *Microwave Theory and Techniques, IEEE Transactions on*, 37(4):669–679, 1989.

[53] M. Abramowitz and I.A. Stegun. *Handbook of mathematical functions: with formulas, graphs, and mathematical tables*, volume 55. Dover publications, 1965.

[54] R. Paknys. Evaluation of hankel functions with complex argument and complex order. *Antennas and Propagation, IEEE Transactions on*, 40(5):569–578, 1992.

[55] HR Park, YM Park, HS Kim, JS Kyoung, MA Seo, DJ Park, YH Ahn, KJ Ahn, and DS Kim. Terahertz nanoresonators: Giant field enhancement and ultrabroadband performance. *Applied Physics Letters*, 96(12):121106–121106, 2010.

[56] HJ Fink and JR Whinnery. Slow waves guided by parallel plane tape guides. *Microwave Theory and Techniques, IEEE Transactions on*, 30(11):2020–2023, 1982.

[57] EN Korshunova, IP Korshunov, AN Sivov, and AD Shatrov. Proper and improper waves of strip with anisotropic conductivity. In *Physics and Engineering of Millimeter and Submillimeter Waves, 1998. MSMW'98. Third International Kharkov Symposium*, volume 1, pages 373–375. IEEE, 1998.

[58] J.M. Jin. *Theory and computation of electromagnetic fields*. Wiley Online Library, 2010.

[59] D. Grischkowsky, S. Keiding, M. Van Exter, and C. Fattinger. Far-infrared time-domain spectroscopy with terahertz beams of dielectrics and semiconductors. *J. Opt. Soc. Am. B*, 7(10):2006–2015, 1990.

[60] R. Mendis and D. Grischkowsky. Undistorted guided-wave propagation of subpicosecond terahertz pulses. *Optics letters*, 26(11):846–848, 2001.

[61] Mohammad Neshat Saman Jafarlou and Safieddin Safavi-Naeini. Green's function approach for analysis of a layered structure with a anisotropic surface. *Manuscript in preparation*.